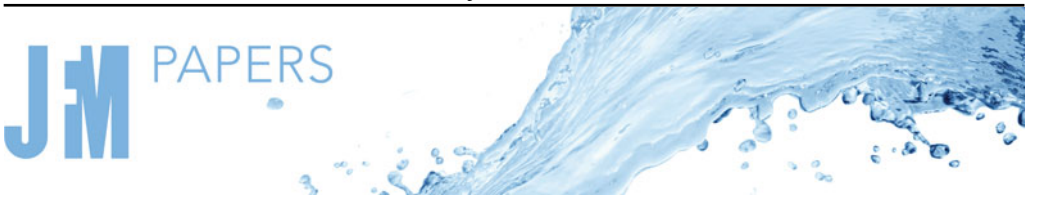
J. Fluid Mech. (2025), *vol.* 1025, A50, doi:10.1017/jfm.2025.10859



Three-dimensional curved shock theory based on orthogonal frame of shock surface and its applications

Mengfei Zhang[1], **Kai Yang**[1], **Chongguang Shi**[1], **Chengxiang Zhu**[1], **Xiaogang Zheng**[1], **Yancheng You**[1] **and Gang Wang**[2]

[1]School of Aerospace Engineering, Xiamen University, Xiamen, Fujian 361005, PR China

[2]Hypervelocity Aerodynamics Institute, China Aerodynamics Research and Development Centre, Mianyang, Sichuan 621000, PR China

Corresponding author: Yancheng You, yancheng.you@xmu.edu.cn

(Received 20 June 2024; revised 14 July 2025; accepted 20 October 2025)

By deriving the Euler equations and Rankine–Hugoniot equations in the orthogonal frame field of the shock surface, the three-dimensional curved shock theory based on orthogonal frame of shock surface (3D-CST-boos) is established. In steady flow, this theory can be applied to three-dimensional (3-D) shocks without constraints on the incoming flow conditions. The derived equations elucidate the relationship between the first-order gradients of the preshock and postshock flow parameters and the geometric properties (curvature) of the 3-D curved shock. The correctness of 3D-CST-boos is verified for two-dimensional plane shocks and axisymmetric shocks. The analysis is then extended to the flow patterns of 3-D elliptical convex/concave shocks. Variations in the flow field behind a 3-D elliptical convex shock are explained based on different incoming flow conditions. Simultaneously, the fundamental mechanics underlying the differences between the flow fields of elliptical concave shocks and axisymmetric concave shocks are revealed using 3D-CST-boos. Finally, a concise analysis of the first-order flow parameters is presented for more complex 3-D shocks, including saddle-shaped shocks and cubic surface shocks.

Key words: shock waves, gas dynamics

1. Introduction

Shock waves are prevalent in various supersonic flow phenomena, significantly influencing the behaviour and dynamics of complex systems. These waves play a pivotal role in diverse fields, from aerospace vehicle design and operation to the exploration of

© The Author(s), 2025. Published by Cambridge University Press. This is an Open Access article, distributed under the terms of the Creative Commons Attribution licence (https://creativecommons.org/licenses/by/4.0/), which permits unrestricted re-use, distribution and reproduction, provided the original article is properly cited.

https://doi.org/10.1017/jfm.2025.10859 Published online by Cambridge University Press

astrophysical phenomena such as supernovae. Therefore, a deeper understanding of the nature and properties of shocks is essential for advancing the field of supersonic flow dynamics. However, the predominant focus of existing shock research revolves around two-dimensional (2-D) flow fields. The zero-order preshock and postshock parameters are established from the Rankine–Hugoniot equations. Crocco (1937) identified a shock point, known as the Crocco point, which prevents streamlines being straight behind the shock. Subsequently, Thomas (1947) demonstrated the existence of a position behind the shock where the pressure gradient along the streamline is zero. Numerous studies, including those by Lin (1948), Hayes (1959), Pant (1971), Emanuel (1988) and Hornung (1998), have explored the impact of the 2-D shock curvature on the first-order gradients of the preshock and postshock flow parameters.

There has been extensive research on 2-D curved shocks, emphasizing the significance of the shock curvature in the supersonic flow field. However, in actual supersonic flow, three-dimensional (3-D) curved shocks are prevalent, and these exhibit more complex geometric characteristics. There is a relatively limited body of study on 3-D curved shocks. To explore this topic, Kanwal (1959) utilized the Gauss–Weingarten formulae in differential geometry to calculate the flow parameter gradient along the postshock streamline in both steady and rotational flows. Serrin (1959) applied the Serret–Frenet equations to 3-D flows, developing a method for determining the gradient of the flow parameters following 3-D curved shocks. This method is applicable only when the pressure gradient is zero in the vertical flow plane. Tembharey (1973) outlined conditions for the existence of complex laminar flows and Beltrami flows behind 3-D stationary curved shocks, while Best (1991) investigated the motion characteristics of 3-D shocks in a variable cross-section flow tube. Hornung (2010) derived the shock jump relation for flows with variable gradients under the condition that a uniformly stable free flow with 3-D curved shocks may trigger an endothermic or exothermic chemical reaction. Mölder (2015) formulated curved shock equations that account for the double curvatures Sa and Sb at any point along the 3-D shock. This groundbreaking work enables theoretical solutions to be derived for the complex problem of 3-D flows. However, these equations are limited to scenarios where the flow plane aligns with the osculating plane, such as in axisymmetric flow fields with a 0° angle of attack (*AOA*). Mölder's theory introduces a novel vorticity equation that considers the impact of preshock non-uniformity and divergence on the vorticity of the postshock region. Filippi (2018) used streamlines behind axisymmetric curved shocks to predict the internal surfaces that produced these streamlines. Expanding on Mölder's curved shock theory, Shi (2020) developed second-order curved shock equations and applied them to the inverse design of flow fields and shock capture. Subsequently, Zhang (2023*a*) combined Mölder's curved shock theory with the method of curved shock characteristics, proposed by Shi (2021), to construct a shock reflection model for planar flow. This model accurately reproduces the structure of shock reflection and Mach reflection in planar flow fields, successfully predicting the shape and height of Mach disks.

Emanuel & Mölder (2021) developed the 3-D curved shock theory for uniformly steady incoming flows. From a geometric perspective, this theory represents a milestone in the solution and analysis of 3-D curved shocks, marking significant importance and value. This theory provides a new thinking angle for us to understand 3-D curved shock, and also provides some enlightenment for 3-D flow analysis and practical applications. It establishes the relationship between the complex curvature features of 3-D curved shocks and the first-order flow parameters behind the shock, demonstrating special parameters (Thomas point, Crocco point, streamline maximum deflection point and sonic line) and vorticity distribution behind the shock using the G-shock as an example. Unlike the streamline coordinate system of Mölder (2015), this theory repositions the coordinate

https://doi.org/10.1017/jfm.2025.10859 Published online by Cambridge University Press

system on the shock surface (as in the establishment of Rankine–Hugoniot equations) and deduces the Euler equation using the orthogonal curvilinear coordinate system of the 3-D space ((43) in Emanuel (2019)). However, to employ an orthogonal coordinate system of the 3-D space ((43) in Emanuel (2019)) on a curved shock surface, it is essential to ensure that the coordinate curves selected on the surface are the principal curves of the surface. Additionally, when performing velocity decomposition along these principal curves of the surface, it is not possible to ensure that one of the velocity components is identically vanishing, which significantly limits the applicability of the 3-D curved shock theory (Emanuel & Mölder (2021)). Furthermore, 3-D curved shocks more commonly occur in non-uniform flow, so it is worth developing the related theory for such scenarios. The 3-D curved shocks encountered in most real flight conditions are highly intricate, and whether the incoming flow is uniform or not significantly impacts the gradients of the postshock parameters. Therefore, there is considerable value in advancing the development of 3-D curved shock theory to encompass more complex 3-D shocks and address the influence of non-uniform incoming flows. The development of relevant theories will not only promote a deeper understanding of 3-D flow fields, but also guide the design of hypersonic vehicles.

This paper derives 3-D curved shock equations in the orthogonal frame field of the shock surface. These equations are applicable to smooth 3-D shocks in either steady uniform or non-uniform incoming flows. Section 2 introduces the specific shock surface coordinate system, where $\boldsymbol{e_l}$ and $\boldsymbol{e_m}$ represent the directions along the shock surface and $\boldsymbol{e_n}$ represents the direction perpendicular to the shock surface. The 3-D Euler equations in the orthogonal frame field of the shock surface are derived, as are the Rankine–Hugoniot equations in partial differential form along the $\boldsymbol{e_l}$ and $\boldsymbol{e_m}$ directions of the shock surface. These equations serve as the core of the 3-D curved shock theory based on orthogonal frame of shock surface (3D-CST-boos). The selection of the orthogonal frame field significantly simplifies the derivation process for the entire set of equations. Moreover, it allows for a clear analysis of the interaction between the flow gradients of the preshock and postshock regions and the shock curvature. In § 3, the $\boldsymbol{e_l}$, κ_{gl} and κ_{nl} variables are eliminated from the 3D-CST-boos governing equations, yielding 2-D curved shock equations. Furthermore, three examples of 2-D shocks are given; the same examples are solved using the method of Mölder (2015), and consistent results are obtained. Additionally, the postshock flow gradients are analysed. Section 4 calculates and analyses the distribution of first-order flow parameters behind an elliptical convex shock. The first-order parameter distribution and flow characteristics behind an elliptical convex shock are then analysed under various flow conditions. Furthermore, the local-turning osculating cones (LTOC) method of Zheng (2020*b*) is used to inversely determine the 3-D flow field formed by an elliptical concave shock, and the flow field information is obtained. The flow field information near the shock is compared with the results of the 3D-CST-boos, and the results are found to be consistent. The fundamental reason for the differences between the elliptical concave shock and axisymmetric concave shock flow fields is revealed. Finally, the 3D-CST-boos governing equations are applied to a saddle-shaped shock and a cubic surface shock.

2. Derivation of 3D-CST-boos

2.1. *Introduction of shock-surface coordinate system*

Significant distinctions exist between 3-D and 2-D shocks. Two-dimensional shocks lack the transverse pressure gradient exhibited by 3-D shocks. As a result, the streamlines within a 3-D flow field experience deflection not only within the osculating plane,

https://doi.org/10.1017/jfm.2025.10859 Published online by Cambridge University Press

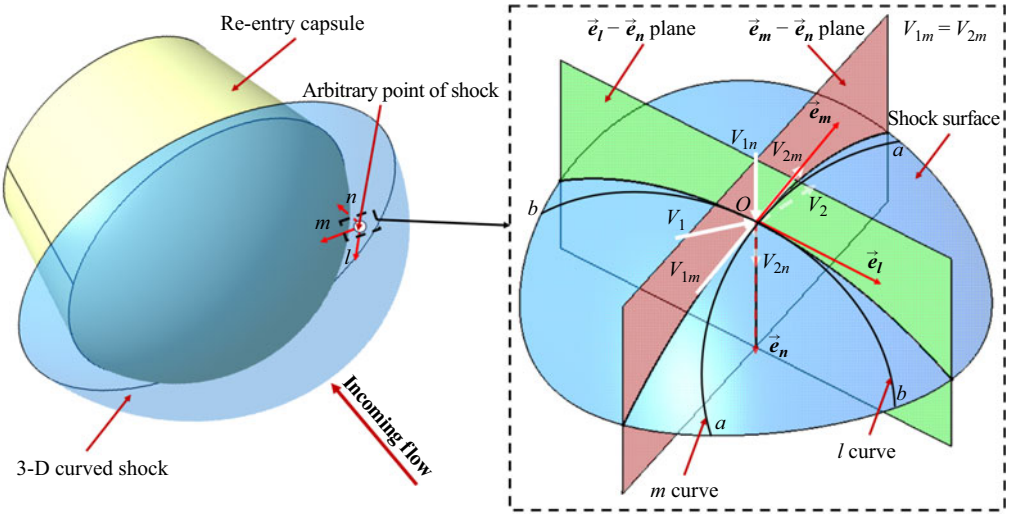


Figure 1. Geometry of 3-D curved shock.

but also in a direction perpendicular to this plane. The transition to a 3-D flow field surpasses the limitations of the conventional flow plane coordinate system. In response, a 3-D curved coordinate system, known as the shock-surface ($\boldsymbol{e_l} - \boldsymbol{e_m} - \boldsymbol{e_n}$) coordinate system (figure 1), has been established. For any continuous and smooth 3-D curved shock, there exists a unique tangent plane at an arbitrary point on the shock surface. In figure 1, when a free incoming flow passes through a 3-D curved shock surface, the upstream velocity vector is V_1 and the downstream velocity vector is V_2. Here V_1 can be decomposed into V_{1m} along the tangent plane and V_{1n} perpendicular to the tangent plane. The direction of V_{1n} is along the $\boldsymbol{e_n}$-axis, that is, the normal vector to the 3-D curved shock. The direction of V_{1m} is along the $\boldsymbol{e_m}$-axis, and the direction perpendicular to the flow plane ($\boldsymbol{e_m} - \boldsymbol{e_n}$ plane) is along the $\boldsymbol{e_l}$-axis. According to the Rankine–Hugoniot equations, the velocity of the $\boldsymbol{e_m}$-axis (along the shock) in front of and behind the shock remains constant. If the process is repeated at other points than O, two curves passing through O and lying on the shock are obtained, namely the m curve and the l curve. On the m curve, the direction of V_{1m} is always the tangent direction of the curve, and the direction of V_{1n} is always the normal direction of the shock surface. On the l curve, the velocity V_{1l} is always zero. In Cheng (2006), the shock surface coordinate system established above is called the orthogonal frame field of a curve on the shock surface in differential geometry. It should be noted that the coordinate curve selected in this paper is the same as that in Emanuel (2019), but the equation used to describe the change of the base vector with the coordinate curve is different. The description equation in Emanuel (2019) is the change equation of the basis vector($\boldsymbol{e_l}$, $\boldsymbol{e_m}$ and $\boldsymbol{e_n}$) in the orthogonal curvilinear coordinate system of the 3-D space (Emanuel 2019, (43)), and the description equation in this paper is the motion equation of the orthogonal frame on a surface. For a shock surface (surface problem, not space problem), if the change equation of the basis vector in the orthogonal curvilinear coordinate system of space (Emanuel 2019, (43)) is to be used in the surface, then the selected coordinate curve on the surface must be the principal curve of the surface. However, only special 3-D surfaces can meet the requirement that the principal curve of the surface coincide with the velocity curve on the surface defined in Emanuel (2019) (the m curve in this paper). The orthogonal frame field of a curve on the shock surface is defined as follows:

https://doi.org/10.1017/jfm.2025.10859 Published online by Cambridge University Press

l curve,

$$\left.\begin{aligned}\partial \boldsymbol{e_l}/\partial l &= \kappa_{gl}\boldsymbol{e_m} + \kappa_{nl}\boldsymbol{e_n},\\ \partial \boldsymbol{e_m}/\partial l &= -\kappa_{gl}\boldsymbol{e_l} + \tau_{gl}\boldsymbol{e_n},\\ \partial \boldsymbol{e_n}/\partial l &= -\kappa_{nl}\boldsymbol{e_l} - \tau_{gl}\boldsymbol{e_m};\end{aligned}\right\} \tag{2.1}$$

m curve,

$$\left.\begin{aligned}\partial \boldsymbol{e_m}/\partial m &= \kappa_{gm}\boldsymbol{e_l} + \kappa_{nm}\boldsymbol{e_n},\\ \partial \boldsymbol{e_l}/\partial m &= -\kappa_{gm}\boldsymbol{e_m} + \tau_{gm}\boldsymbol{e_n},\\ \partial \boldsymbol{e_n}/\partial m &= -\kappa_{nm}\boldsymbol{e_m} - \tau_{gm}\boldsymbol{e_l}.\end{aligned}\right\} \tag{2.2}$$

In the above definition, κ_{gl}, κ_{nl}, τ_{gl}, κ_{gm}, κ_{nm} and τ_{gm} are related to the curvature of a 3-D shock surface. Here κ_{nm} is the normal curvature of the shock surface along the direction m of the curve, κ_{nl} is the normal curvature of the shock surface along the direction l of the curve, κ_{gl} is the geodesic curvature of the curve l on the shock surface, κ_{gm} is the geodesic curvature of the curve m on the shock surface, τ_{gm} is the geodesic torsion of the curve m on the shock surface and τ_{gl} is the geodesic torsion of the curve l on the shock surface. Take the calculation of κ_{gl} as an example:

$$\kappa_{gl} = \frac{\partial \boldsymbol{e_l}}{\partial l}\boldsymbol{e_m} = \left(\frac{\partial \boldsymbol{e_l}}{\partial x}\frac{\partial x}{\partial l} + \frac{\partial \boldsymbol{e_l}}{\partial y}\frac{\partial y}{\partial l} + \frac{\partial \boldsymbol{e_l}}{\partial z}\frac{\partial z}{\partial l}\right)\boldsymbol{e_m}. \tag{2.3}$$

When the equation $F(x, y, z)$ of the shock surface is given, the coordinates of any point O on the shock surface are (x_0, y_0, z_0). And expressions for $\boldsymbol{e_l}(x, y, z)$, $\boldsymbol{e_m}(x, y, z)$ and $\boldsymbol{e_n}(x, y, z)$ based on point O can be determined. By substituting the coordinates of point O into the expressions for $\boldsymbol{e_l}(x, y, z)$, $\boldsymbol{e_m}(x, y, z)$ and $\boldsymbol{e_n}(x, y, z)$, the value of the curvature dependent term κ_{gl} can be found.

From the above definition, the velocity vector is

$$\boldsymbol{V} = V_l\boldsymbol{e_l} + V_m\boldsymbol{e_m} + V_n\boldsymbol{e_n}. \tag{2.4}$$

2.2. *Shock-surface coordinate transformation of Euler equations*

At positions away from the shock, the flow is assumed to be steady, non-viscous and adiabatic. The Euler equations can clearly describe the flow in space through the following basic equations:

$$\left.\begin{aligned}&\text{mass conservation equation} \quad \nabla\cdot(\rho\boldsymbol{V}) = 0,\\ &\text{momentum equation} \quad \rho\boldsymbol{V}\cdot\nabla\boldsymbol{V} + \nabla p = 0,\\ &\text{energy equation} \quad \rho\,(\boldsymbol{V}\cdot\nabla)\left(h + \frac{V^2}{2}\right) = 0.\end{aligned}\right\} \tag{2.5}$$

The general expression of the Euler equations above can be expanded to the shock surface coordinate system. The velocity defined in § 2.1 is introduced to the derivation. The details can be found in Appendix A; only the final equations are given here:

mass conservation equation,

$$\rho\frac{\partial V_m}{\partial m} + \rho\frac{\partial V_n}{\partial n} + V_m\frac{\partial \rho}{\partial m} + V_n\frac{\partial \rho}{\partial n} - \rho V_n\kappa_{nm} - \rho V_n\kappa_{nl} - \rho V_m\kappa_{gl} = 0; \tag{2.6}$$

https://doi.org/10.1017/jfm.2025.10859 Published online by Cambridge University Press

momentum equations,

$$\boldsymbol{e_l}:\rho V_n\frac{\partial V_l}{\partial n}+\rho V_m^2\kappa_{gm}-\rho V_m V_n\tau_{gm}+\frac{\partial p}{\partial l}=0, \tag{2.7}$$

$$\boldsymbol{e_m}:\rho V_m\frac{\partial V_m}{\partial m}+\rho V_n\frac{\partial V_m}{\partial n}-\rho V_n V_m\kappa_{nm}+\frac{\partial p}{\partial m}=0, \tag{2.8}$$

$$\boldsymbol{e_n}:\rho V_n\frac{\partial V_n}{\partial n}+\rho V_m\frac{\partial V_n}{\partial m}+\rho V_m^2\kappa_{nm}+\frac{\partial p}{\partial n}=0; \tag{2.9}$$

energy equation,

$$\begin{aligned}&\frac{\gamma V_m}{\gamma-1}\left(\frac{\partial p}{\partial m}-\frac{p}{\rho}\frac{\partial \rho}{\partial m}\right)+\rho V_m^2\frac{\partial V_m}{\partial m}+\rho V_m V_n\frac{\partial V_n}{\partial m}\\&\quad+\frac{\gamma V_n}{\gamma-1}\left(\frac{\partial p}{\partial n}-\frac{p}{\rho}\frac{\partial \rho}{\partial n}\right)+\rho V_n V_m\frac{\partial V_m}{\partial n}+\rho V_n^2\frac{\partial V_n}{\partial n}=0.\end{aligned} \tag{2.10}$$

The partial derivatives of the equation of state $P=\rho RT$ along the $\boldsymbol{e_l}$, $\boldsymbol{e_m}$ and $\boldsymbol{e_n}$ directions are expressed as follows:

$$\boldsymbol{e_l}:\frac{\partial p}{\partial l}=\frac{\partial \rho}{\partial l}RT+\rho R\frac{\partial T}{\partial l}, \tag{2.11}$$

$$\boldsymbol{e_m}:\frac{\partial p}{\partial m}=\frac{\partial \rho}{\partial m}RT+\rho R\frac{\partial T}{\partial m}, \tag{2.12}$$

$$\boldsymbol{e_n}:\frac{\partial p}{\partial n}=\frac{\partial \rho}{\partial n}RT+\rho R\frac{\partial T}{\partial n}. \tag{2.13}$$

In the above equations, there exist 21 unknown parameters, namely $\partial p/\partial l$, $\partial p/\partial m$, $\partial p/\partial n$, $\partial T/\partial l$, $\partial T/\partial m$, $\partial T/\partial n$, $\partial \rho/\partial l$, $\partial \rho/\partial m$, $\partial \rho/\partial n$, $\partial V_m/\partial l$, $\partial V_m/\partial m$, $\partial V_m/\partial n$, $\partial V_n/\partial l$, $\partial V_n/\partial m$, $\partial V_n/\partial n$, $\partial V_l/\partial n$, κ_{nm}, κ_{nl}, κ_{gl}, κ_{gm} and τ_{gm}. By considering the partial derivatives $\partial p/\partial l$, $\partial p/\partial m$, $\partial V_m/\partial l$, $\partial V_m/\partial m$, $\partial V_n/\partial l$, $\partial V_n/\partial m$, $\partial \rho/\partial l$, $\partial \rho/\partial m$ and the curvature values κ_{nm}, κ_{nl}, κ_{gl}, κ_{gm} , τ_{gm} at any point of a 3-D curved shock surface, it is feasible to determine the remaining unknown parameters using a combination of the eight (2.6)–(2.13) and the 13 given parameters. The partial derivatives $\partial V_l/\partial l$ and $\partial V_l/\partial m$ are both zero. This is because the definition of the coordinate system at any point on the 3-D curved shock relies on the velocity decomposition method, where the magnitude of V_l is always zero on the shock surface. Consequently, the potential (partial derivative) of V_l in any direction along the shock surface is also zero.

2.3. *Derivation of 3D-CST-boos equations*

The Rankine–Hugoniot equations are important in describing the preshock and postshock flow parameters. The specific expressions are

$$\left.\begin{aligned}&\rho_1 V_{1n}=\rho_2 V_{2n},\\&p_1+\rho_1 V_{1n}^2=p_2+\rho_2 V_{2n}^2,\\&V_{1m}=V_{2m},\\&\frac{\gamma RT_1}{\gamma-1}+\frac{\left(V_{1n}^2+V_{1m}^2\right)}{2}=\frac{\gamma RT_2}{\gamma-1}+\frac{\left(V_{2n}^2+V_{2m}^2\right)}{2},\\&\frac{p_1}{\rho_1 T_1}=\frac{p_2}{\rho_2 T_2}.\end{aligned}\right\} \tag{2.14}$$

https://doi.org/10.1017/jfm.2025.10859 Published online by Cambridge University Press

In the above equations, the subscript '1' represents the preshock flow parameters and the subscript '2' represents the postshock flow parameters. The subscripts n and m are consistent with the subscripts n and t in the oblique shock relations in the general literature. The partial derivative relations in the $\boldsymbol{e_l}$ and $\boldsymbol{e_m}$ directions near the shock are derived by applying the equations of mass conservation, momentum conservation and the condition $V_{1m} = V_{2m}$ stated in the Rankine–Hugoniot equations. The resulting equations governing these relations are presented as follows:

mass conservation equations,

$$\boldsymbol{e_l}: V_{1n}\frac{\partial \rho_1}{\partial l} + \frac{\partial V_{1n}}{\partial l}\rho_1 = V_{2n}\frac{\partial \rho_2}{\partial l} + \frac{\partial V_{2n}}{\partial l}\rho_2, \tag{2.15}$$

$$\boldsymbol{e_m}: V_{1n}\frac{\partial \rho_1}{\partial m} + \frac{\partial V_{1n}}{\partial m}\rho_1 = V_{2n}\frac{\partial \rho_2}{\partial m} + \frac{\partial V_{2n}}{\partial m}\rho_2; \tag{2.16}$$

momentum equations,

$$\boldsymbol{e_l}: \frac{\partial p_1}{\partial l} + V_{1n}^2\frac{\partial \rho_1}{\partial l} + 2\rho_1 V_{1n}\frac{\partial V_{1n}}{\partial l} = \frac{\partial p_2}{\partial l} + V_{2n}^2\frac{\partial \rho_2}{\partial l} + 2\rho_2 V_{2n}\frac{\partial V_{2n}}{\partial l}, \tag{2.17}$$

$$\boldsymbol{e_m}: \frac{\partial p_1}{\partial m} + V_{1n}^2\frac{\partial \rho_1}{\partial m} + 2\rho_1 V_{1n}\frac{\partial V_{1n}}{\partial m} = \frac{\partial p_2}{\partial m} + V_{2n}^2\frac{\partial \rho_2}{\partial m} + 2\rho_2 V_{2n}\frac{\partial V_{2n}}{\partial m}; \tag{2.18}$$

velocity relations,

$$\boldsymbol{e_l}: \frac{\partial V_{1m}}{\partial l} = \frac{\partial V_{2m}}{\partial l}, \tag{2.19}$$

$$\boldsymbol{e_m}: \frac{\partial V_{1m}}{\partial m} = \frac{\partial V_{2m}}{\partial m}; \tag{2.20}$$

energy relations,

$$\boldsymbol{e_l}: \frac{\gamma}{\gamma-1}\left(\frac{1}{\rho_1}\frac{\partial p_1}{\partial l} - \frac{p_1}{\rho_1^2}\frac{\partial \rho_1}{\partial l}\right) + V_{1n}\frac{\partial V_{1n}}{\partial l} = \frac{\gamma}{\gamma-1}\left(\frac{1}{\rho_2}\frac{\partial p_2}{\partial l} - \frac{p_2}{\rho_2^2}\frac{\partial \rho_2}{\partial l}\right) + V_{2n}\frac{\partial V_{2n}}{\partial l}, \tag{2.21}$$

$$\boldsymbol{e_m}: \frac{\gamma}{\gamma-1}\left(\frac{1}{\rho_1}\frac{\partial p_1}{\partial m} - \frac{p_1}{\rho_1^2}\frac{\partial \rho_1}{\partial m}\right) + V_{1n}\frac{\partial V_{1n}}{\partial m} = \frac{\gamma}{\gamma-1}\left(\frac{1}{\rho_2}\frac{\partial p_2}{\partial m} - \frac{p_2}{\rho_2^2}\frac{\partial \rho_2}{\partial m}\right) + V_{2n}\frac{\partial V_{2n}}{\partial m}. \tag{2.22}$$

Equations (2.15)–(2.22) establish the relationship between the partial first-order preshock and postshock flow parameters. The governing equations for the flow field prior to and following the shock are represented by (2.6)–(2.13). In total, there are 24 governing equations that account for both preshock and postshock scenarios. These equations include the partial derivatives of p_1, ρ_1, T_1, V_{1m}, V_{1n}, p_2, ρ_2, T_2, V_{2m} and V_{2n} with respect to the directions $\boldsymbol{e_l}$, $\boldsymbol{e_m}$, $\boldsymbol{e_n}$ and the partial derivatives of V_{1l} and V_{2l} with respect to the directions $\boldsymbol{e_n}$, along with the geometric parameters κ_{nm}, κ_{nl}, κ_{gl}, κ_{gm} and τ_{gm}. Collectively, therefore, there are 37 unknowns. By combining the eight (2.15)–(2.22) derived in this section to describe the phenomena across the shock, a set of 24 equations portrays the complete 3-D flow field that encompasses the presence of shocks. Moreover, if 13 of these 37 unknowns are known, the remaining 24 can be determined using these 24 equations.

Based on this set of 24 equations, three distinct applications are considered. The first involves determining the first-order information of all parameters in the preshock and postshock states when the eight flow partial derivatives at any given point on the preshock

https://doi.org/10.1017/jfm.2025.10859 Published online by Cambridge University Press

surface are known. These partial derivatives are $\partial p_1/\partial l$, $\partial p_1/\partial m$, $\partial V_{1m}/\partial l$, $\partial V_{1m}/\partial m$, $\partial V_{1n}/\partial l$, $\partial V_{1n}/\partial m$, $\partial \rho_1/\partial l$ and $\partial \rho_1/\partial m$, along with the shock curvatures κ_{nm}, κ_{nl}, κ_{gl}, κ_{gm} and τ_{gm} at that particular point. When the zero-order parameters are known, these 24 equations enable the acquisition of the first-order information for all preshock and postshock parameters. The second application entails obtaining the gradients of the flow parameters in the preshock state when the eight flow partial derivatives along the shock surface behind a 3-D curved shock and the shock curvatures are known. In the third application, assuming that 13 partial derivatives of the preshock and postshock conditions are known, such as $\partial p_1/\partial l, \partial p_1/\partial m, \partial p_1/\partial n, \partial \rho_1/\partial l, \partial \rho_1/\partial m, \partial \rho_1/\partial n, \partial T_1/\partial l, \partial T_1/\partial m$, $\partial T_1/\partial n$, $\partial p_2/\partial l$, $\partial p_2/\partial m$, $\partial \rho_2/\partial l$ and $\partial \rho_2/\partial m$, the curvatures κ_{nm}, κ_{nl}, κ_{gl}, κ_{gm} and τ_{gm} can be determined at any point on the shock surface using the set of 24 equations. The theoretical framework established here has implications for investigating 3-D shock reflection and shock-capture phenomena. Second-order curved shock theory (Shi 2021) is applied to shock capture and reflection shock solution, and the higher-order parameters obtained can be used to obtain more accurate shock, reflection structure and reflection flow field. This is also a possible application direction of 3D-CST-boos. The precise construction of a 3-D shock shape can be achieved by leveraging the first-order information of both the preshock and postshock states.

Subsequently, a detailed derivation of the first application of the 3D-CST-boos governing equations is presented. Extensive research has been conducted on the flow condition behind the shock when the incoming flow parameters are specified. Notably, the characteristics of the postshock flow field, particularly the Crocco point and Thomas point, have garnered significant attention.

The Crocco point and Thomas point are closely associated with the pressure gradient in the postshock region. To determine the pressure gradient in the $\boldsymbol{e_l}$, $\boldsymbol{e_m}$, and $\boldsymbol{e_n}$ directions following the shock, the eight gradient values along the preshock region are provided, namely $\partial p_1/\partial l$, $\partial p_1/\partial m$, $\partial V_{1m}/\partial l$, $\partial V_{1m}/\partial m$, $\partial V_{1n}/\partial l$, $\partial V_{1n}/\partial m$, $\partial \rho_1/\partial l$ and $\partial \rho_1/\partial m$. These gradient values encompass both uniform and non-uniform incoming flows. Subsequently, (2.15)–(2.22) are simplified to offer a more intuitive representation of the influence of the known preshock gradient parameters on the unknown postshock gradient parameters.

The process of establishing a coordinate system does not involve parametric equations for surfaces, so the characteristic lengths of l, m and n are specified here as arclengths. The dimensionless pressure gradient and velocity gradient are defined as follows:

$$\text{pressure,} \quad \frac{\partial p}{p\partial l} = P_L, \quad \frac{\partial p}{p\partial m} = P_M, \quad \frac{\partial p}{p\partial n} = P_N; \tag{2.23}$$

$$\text{density,} \quad \frac{\partial \rho}{\rho\partial l} = R_L, \quad \frac{\partial \rho}{\rho\partial m} = R_M, \quad \frac{\partial \rho}{\rho\partial n} = R_N; \tag{2.24}$$

$$\text{velocity,} \quad \frac{\partial V_m}{V_m\partial l} = V_{ML}, \quad \frac{\partial V_m}{V_m\partial m} = V_{MM}, \quad \frac{\partial V_n}{V_n\partial l} = V_{NL}, \quad \frac{\partial V_n}{V_n\partial m} = V_{NM}. \tag{2.25}$$

The following expressions are obtained:

mass conservation equations,

$$R_{1L} + V_{1NL} = R_{2L} + V_{2NL}, \tag{2.26}$$

$$R_{1M} + V_{1NM} = R_{2M} + V_{2NM}; \tag{2.27}$$

momentum equations,

$$A_1P_{1L} + B_1R_{1L} + 2B_1V_{1NL} = A_2P_{2L} + B_2R_{2L} + 2B_2V_{2NL}, \tag{2.28}$$

$$A_1P_{1M} + B_1R_{1M} + 2B_1V_{1NM} = A_2P_{2M} + B_2R_{2M} + 2B_2V_{2NM}; \tag{2.29}$$

https://doi.org/10.1017/jfm.2025.10859 Published online by Cambridge University Press

velocity relations,

$$V_{1ML} = V_{2ML}, \tag{2.30}$$
$$V_{1MM} = V_{2MM}; \tag{2.31}$$

energy relations,

$$C_1 P_{1L} - C_1 R_{1L} + D_1 V_{1NL} = C_2 P_{2L} - C_2 R_{2L} + D_2 V_{2NL}, \tag{2.32}$$
$$C_1 P_{1M} - C_1 R_{1M} + D_1 V_{1NM} = C_2 P_{2M} - C_2 R_{2M} + D_2 V_{2NM}. \tag{2.33}$$

Where the influence coefficients are

$$\left.\begin{aligned} A_1 &= p_1, \quad & B_1 &= V_{1n}^2 \rho_1, \\ A_2 &= p_2, \quad & B_2 &= V_{2n}^2 \rho_2, \\ C_1 &= \frac{\gamma}{\gamma - 1}\frac{p_1}{\rho_1}, \quad & D_1 &= V_{1n}^2, \\ C_2 &= \frac{\gamma}{\gamma - 1}\frac{p_2}{\rho_2}, \quad & D_2 &= V_{2n}^2. \end{aligned}\right\} \tag{2.34}$$

Further simplification allows the direct expressions of the dimensionless velocity, pressure and density gradients to be expressed as follows along the postshock surface. For a detailed explanation of the specific simplification process, see Appendix B. The final equations are presented as follows:

$$P_{2L} = J_1 R_{1L} + J_2 V_{1NL} + J_3 P_{1L}, \tag{2.35}$$
$$P_{2M} = J_1 R_{1M} + J_2 V_{1NM} + J_3 P_{1M}, \tag{2.36}$$
$$R_{2L} = (1 + K_1) R_{1L} + K_2 P_{1L} + K_3 V_{1NL}, \tag{2.37}$$
$$R_{2M} = (1 + K_1) R_{1M} + K_2 P_{1M} + K_3 V_{1NM}, \tag{2.38}$$
$$V_{2NL} = -K_1 R_{1L} - K_2 P_{1L} - K_3 V_{1NL}, \tag{2.39}$$
$$V_{2NM} = -K_1 R_{1M} - K_2 P_{1M} - K_3 V_{1NM}. \tag{2.40}$$

The coefficients can be expressed as

$$\left.\begin{aligned} J_1 &= \left(-\frac{B_2}{A_2} + \frac{-B_2 A_2 C_2 - B_2^2 C_2 + B_1 B_2 C_2}{A_2^2 D_2 + A_2^2 C_2 - A_2 B_2 C_2} + \frac{B_1}{A_2} + \frac{B_2 C_1}{A_2 D_2 + A_2 C_2 - B_2 C_2}\right), \\ J_2 &= \left(-\frac{B_2}{A_2} + \frac{-B_2 A_2 C_2 - B_2^2 C_2}{A_2^2 D_2 + A_2^2 C_2 - A_2 B_2 C_2} + \frac{2B_1}{A_2} + \frac{2B_1 B_2 C_2 - B_2 A_2 D_1}{A_2^2 D_2 + A_2^2 C_2 - A_2 B_2 C_2}\right), \\ J_3 &= \left(\frac{A_1}{A_2} + \frac{A_1 B_2 C_2 - A_2 B_2 C_1}{A_2^2 D_2 + A_2^2 C_2 - A_2 B_2 C_2}\right), \\ K_1 &= \left(\frac{-A_2 C_2 - B_2 C_2}{A_2 D_2 + A_2 C_2 - B_2 C_2} + \frac{B_1 C_2 + A_2 C_1}{A_2 D_2 + A_2 C_2 - B_2 C_2}\right), \\ K_2 &= \left(\frac{B_1 C_2 + A_2 C_1}{A_2 D_2 + A_2 C_2 - B_2 C_2}\right), \\ K_3 &= \left(\frac{-A_2 C_2 - B_2 C_2 + 2B_1 C_2 - A_2 D_1}{A_2 D_2 + A_2 C_2 - B_2 C_2}\right). \end{aligned}\right\} \tag{2.41}$$

Equations (2.35)–(2.40) reveal the direct relationship between the first-order preshock and postshock parameters. Through the analysis of the above equation, it can be found that

https://doi.org/10.1017/jfm.2025.10859 Published online by Cambridge University Press

P_{2L}, R_{2L} and V_{2NL} in the $\boldsymbol{e_l}$ direction behind the shock are related only to P_{1L}, R_{1L} and V_{1NL} in the $\boldsymbol{e_l}$ direction before the shock. The same principle applies to the $\boldsymbol{e_m}$ direction.

To determine the precise locations of the Crocco and Thomas points in the postshock region, the pressure gradient in the $\boldsymbol{e_n}$ direction behind the shock must be derived. By employing the Euler (2.6)–(2.13) behind the shock, the equation for P_{2N} can be obtained. For a step-by-step derivation process, see Appendix C. The resulting expression is as follows:

$$P_{2N} = L_1 P_{2M} + L_2 \left(V_{2MM} - V_{2NM}\right) - L_2 \kappa_{gl} - L_3 \left(\kappa_{nl} + \kappa_{nm}\right) - L_4 \kappa_{nm}. \tag{2.42}$$

Where the coefficients can be expressed as

$$\left.\begin{aligned} L_1 &= \frac{V_{2m}}{V_{2n}} \Big/ \left(\frac{\gamma p_2}{\rho_2 V_{2n}^2} - 1\right), \quad L_2 = \frac{\gamma V_{2m}}{V_{2n}} \Big/ \left(\frac{\gamma p_2}{\rho_2 V_{2n}^2} - 1\right), \\ L_3 &= \gamma \Big/ \left(\frac{\gamma p_2}{\rho_2 V_{2n}^2} - 1\right), \quad L_4 = \frac{\gamma V_{2m}^2}{V_{2n}^2} \Big/ \left(\frac{\gamma p_2}{\rho_2 V_{2n}^2} - 1\right). \end{aligned}\right\} \tag{2.43}$$

Equation (2.42) describes the relationship between the gradient parameters behind the shock. Furthermore, (2.42) can be converted into the following expression using (2.31), (2.36) and (2.40):

$$\begin{aligned} P_{2N} = {} & (L_1 J_1 + L_2 K_1) R_{1M} + (L_1 J_2 + L_2 K_3) V_{1NM} + (L_1 J_3 + L_2 K_2) P_{1M} \\ & + L_2 V_{1MM} - L_2 \kappa_{gl} - L_3 \left(\kappa_{nl} + \kappa_{nm}\right) - L_4 \kappa_{nm}. \end{aligned} \tag{2.44}$$

It is clear from (2.44) that the postshock pressure gradient in the $\boldsymbol{e_n}$ direction is directly related to the preshock pressure gradient in the $\boldsymbol{e_m}$ direction, the preshock velocity V_{1n} gradient in the $\boldsymbol{e_m}$ direction, the preshock density gradient in the $\boldsymbol{e_m}$ direction and the shock curvatures.

Further, the expression of the pressure gradient behind the shock is summarized as follows:

$$\begin{aligned} P_{2L} &= J_1 R_{1L} + J_2 V_{1NL} + J_3 P_{1L}, \\ P_{2M} &= J_1 R_{1M} + J_2 V_{1NM} + J_3 P_{1M}, \\ P_{2N} &= (L_1 J_1 + L_2 K_1) R_{1M} + (L_1 J_2 + L_2 K_3) V_{1NM} + (L_1 J_3 + L_2 K_2) P_{1M} \\ &\quad + L_2 V_{1MM} - L_2 \kappa_{gl} - L_3 \left(\kappa_{nl} + \kappa_{nm}\right) - L_4 \kappa_{nm}. \end{aligned} \tag{2.45}$$

The pressure gradient at any point behind the 3-D curved shock can be written as

$$\nabla p_2 = \left[\frac{\partial p_2}{\partial l}, \frac{\partial p_2}{\partial m}, \frac{\partial p_2}{\partial n}\right]. \tag{2.46}$$

The following expressions are used to project ∇p_2:

$$P = \frac{\nabla p \cdot \boldsymbol{V}}{\rho V^3} \cdot \frac{\boldsymbol{V}}{V}, \tag{2.47}$$

$$D = \frac{\nabla p}{\rho V^2} - P. \tag{2.48}$$

Here, the definitions of Emanuel & Mölder (2021) are adopted, with the pressure gradient along the streamline being P and the curvature of the streamline being D. The point at which $P_2 = 0$ is the location of the Thomas point, and $D_2 = 0$ is gives the location of the Crocco point.

https://doi.org/10.1017/jfm.2025.10859 Published online by Cambridge University Press

3. Using 2D-CST to verify the correctness of 3D-CST-boos in 2-D shocks

This section employs Mölder's (2015) equations to validate the accuracy of 3D-CST-boos when applied to solving 2-D curved shock problems. The simplification process from 3D-CST-boos to 2-D curved shock theory is outlined, accompanied by three examples for verification.

3.1. *Simplification of 3D-CST-boos to the 2-D curved shock equations*

By disregarding the correlation equations and parameters in the $\boldsymbol{e_l}$ direction, the 3D-CST-boos equations can be simplified to the 2-D curved shock equations. Prior studies of Hornung (1998), Mölder (2015) and Emanuel (2019) often categorized 2-D planar flow and axisymmetric flow as 2-D from a flow perspective. However, from a geometric standpoint, axisymmetric shocks retain 3-D geometry traits. Therefore, the equations presented in § 2.3 directly provide solutions for axisymmetric shocks. This section focuses on deriving the 2-D curved shock equations. The governing equations of flows before and behind the shock are expressed in the $\boldsymbol{e_m}$ and $\boldsymbol{e_n}$ directions as follows:

mass conservation equation,

$$\rho\frac{\partial V_m}{\partial m}+\rho\frac{\partial V_n}{\partial n}+V_m\frac{\partial \rho}{\partial m}+V_n\frac{\partial \rho}{\partial n}-\rho V_n\kappa_{nm}=0; \tag{3.1}$$

momentum equations,

$$\boldsymbol{e_m}:\rho V_m\frac{\partial V_m}{\partial m}+\rho V_n\frac{\partial V_m}{\partial n}-\rho V_nV_m\kappa_{nm}+\frac{\partial p}{\partial m}=0, \tag{3.2}$$

$$\boldsymbol{e_n}:\rho V_n\frac{\partial V_n}{\partial n}+\rho V_m\frac{\partial V_n}{\partial m}+\rho V_m^2\kappa_{nm}+\frac{\partial p}{\partial n}=0; \tag{3.3}$$

energy equation,

$$\begin{aligned}&\frac{\gamma V_m}{\gamma-1}\left(\frac{\partial p}{\partial m}-\frac{p}{\rho}\frac{\partial \rho}{\partial m}\right)+\rho V_m^2\frac{\partial V_m}{\partial m}+\rho V_mV_n\frac{\partial V_n}{\partial m}\\&\quad+\frac{\gamma V_n}{\gamma-1}\left(\frac{\partial p}{\partial n}-\frac{p}{\rho}\frac{\partial \rho}{\partial n}\right)+\rho V_nV_m\frac{\partial V_m}{\partial n}+\rho V_n^2\frac{\partial V_n}{\partial n}=0;\end{aligned} \tag{3.4}$$

state equations,

$$\boldsymbol{e_m}:\frac{\partial p}{\partial m}=\frac{\partial \rho}{\partial m}RT+\rho R\frac{\partial T}{\partial m}, \tag{3.5}$$

$$\boldsymbol{e_n}:\frac{\partial p}{\partial n}=\frac{\partial \rho}{\partial n}RT+\rho R\frac{\partial T}{\partial n}. \tag{3.6}$$

Compared with (2.6)–(2.13), (3.1)–(3.6) simply remove the $\boldsymbol{e_l}$ direction marker, κ_{nl} and κ_{gl}, which reflects the compatibility of the 3D-CST-boos equations. The partial derivatives of the conservation of mass, conservation of momentum and $V_{1m}=V_{2m}$ in the Rankine–Hugoniot equations along the $\boldsymbol{e_m}$ direction of the shock tangent line are calculated as follows:

$$V_{1n}\frac{\partial \rho_1}{\partial m}+\frac{\partial V_{1n}}{\partial m}\rho_1=V_{2n}\frac{\partial \rho_2}{\partial m}+\frac{\partial V_{2n}}{\partial m}\rho_2, \tag{3.7}$$

$$\frac{\partial p_1}{\partial m}+V_{1n}^2\frac{\partial \rho_1}{\partial m}+2\rho_1V_{1n}\frac{\partial V_{1n}}{\partial m}=\frac{\partial p_2}{\partial m}+V_{2n}^2\frac{\partial \rho_2}{\partial m}+2\rho_2V_{2n}\frac{\partial V_{2n}}{\partial m}, \tag{3.8}$$

$$\frac{\partial V_{1m}}{\partial m}=\frac{\partial V_{2m}}{\partial m}, \tag{3.9}$$

https://doi.org/10.1017/jfm.2025.10859 Published online by Cambridge University Press

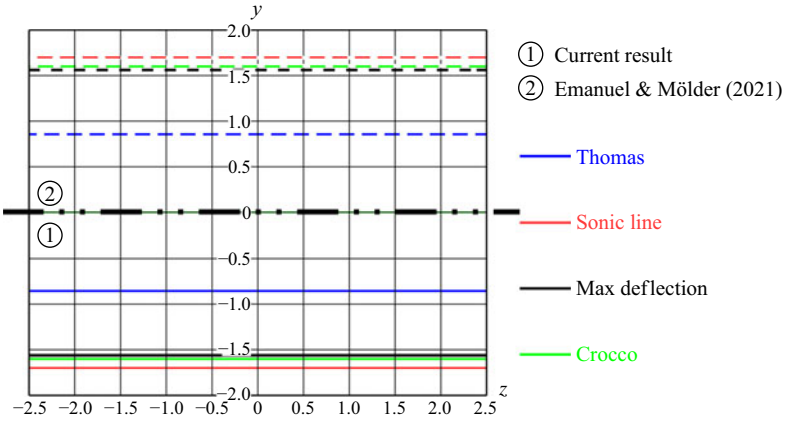


Figure 2. Special conditions at back of planar shock ($f = ((x+6)^2/9) - (y^2/9) - 1 = 0$) at Mach 3.

$$\frac{\gamma}{\gamma-1}\left(\frac{1}{\rho_1}\frac{\partial p_1}{\partial m} - \frac{p_1}{\rho_1^2}\frac{\partial \rho_1}{\partial m}\right) + V_{1n}\frac{\partial V_{1n}}{\partial m} = \frac{\gamma}{\gamma-1}\left(\frac{1}{\rho_2}\frac{\partial p_2}{\partial m} - \frac{p_2}{\rho_2^2}\frac{\partial \rho_2}{\partial m}\right) + V_{2n}\frac{\partial V_{2n}}{\partial m}. \tag{3.10}$$

The governing equations for the preshock and postshock conditions are represented by (3.1)–(3.6), where the subscript '1' denotes preshock and the subscript '2' denotes postshock. Combined with shock relation (3.7)–(3.10), a set of 16 equations is obtained. Within these equations, there are 21 unknowns: partial derivatives of p_1, ρ_1, T_1, V_{1m}, V_{1n}, p_2, ρ_2, T_2, V_{2m} and V_{2n} along the $\boldsymbol{e_m}$ and $\boldsymbol{e_n}$ directions, and the curvature κ_{nm}. By providing five known quantities, the remaining unknowns can be determined. Applying the derivation process outlined in § 2.3 to (3.1)–(3.10) yields the pressure gradient expression. The same results as Mölder (2015) can be obtained by decomposing the P_{2M} and P_{2N} directions along the streamlines and the curvature of the streamlines:

$$P_{2M} = J_1 R_{1M} + J_2 V_{1NM} + J_3 P_{1M}, \tag{3.11}$$

$$P_{2N} = (L_1 J_1 + L_2 K_1) R_{1M} + (L_1 J_2 + L_2 K_3) V_{1NM} + (L_1 J_3 + L_2 K_2) P_{1M} + L_2 V_{1MM} - L_3 \kappa_{nm} - L_4 \kappa_{nm}. \tag{3.12}$$

Upon comparing the 2-D and 3-D curved shock equations, the sole disparity is in the term κ_{nl} and κ_{gl}. Analysis of (2.6) indicates that κ_{nm} induces contraction/expansion of the flow field along the $\boldsymbol{e_l}$ and $\boldsymbol{e_n}$ directions, causing changes in the first-order parameters of the flow field; κ_{nl} and κ_{gl} exerts a similar influence.

3.2. *Comparison with 2-D curved shock*

As the shock curvature κ_{nl} and κ_{gl} approaches zero, a unique case appears of a 3-D curved shock in which the shock surface flattens remarkably along the vertical streamline direction. Treating this situation as a 2-D problem, figure 2 illustrates the distribution of specific parameters for an incoming Mach number of $M_1 = 3$, with the shock shape defined by

$$f = \frac{(x+6)^2}{9} - \frac{y^2}{9} - 1 = 0. \tag{3.13}$$

In the figure, the blue line represents the Thomas point, indicating $P_2 = 0$. The green line, denoting the Crocco point with $D_2 = 0$, indicates that the streamline behind the shock is straight. The red line marks the sonic position, serving as the boundary between

https://doi.org/10.1017/jfm.2025.10859 Published online by Cambridge University Press

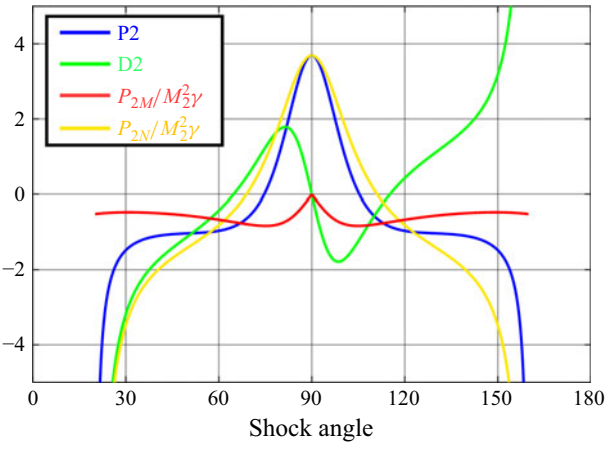


Figure 3. Pressure gradient and flow curvature behind a planar convex shock ($\kappa_{nm} = -1$).

supersonic and subsonic regions, while the black line represents the position of maximum deflection. The symmetry of the shock with respect to the $y = 0$ plane means that the special parameter behind the shock also exhibits symmetry with respect to this plane. The results obtained using the method of Emanuel & Mölder (2021) are shown as dashed lines. A comparison between the solid and dotted lines demonstrates that the special parameters align precisely. Thus, the 3-D curved shock equations derived in this study can be used to resolve the 2-D shock problem.

Our analysis focuses on a distinctive 2-D shock known as a convex shock with a curvature κ_{nm} of -1. Figure 3 illustrates the changes in pressure gradient along the streamline P_2 (blue line), flow curvature gradient D_2 (green line), pressure gradient along the shock surface $P_{2M}/M_2^2\gamma$ (red line) and shock surface normal gradient $P_{2N}/M_2^2\gamma$ (orange line) as a function of the shock angle. The Thomas and Crocco points correspond to the locations where P_2 and D_2 become zero. The directions of the pressure gradient in the $\boldsymbol{e_m}$ and $\boldsymbol{e_n}$ orientations are defined in relation to the coordinate system, where positive and negative values are associated with distinct directions. For the convex shock under consideration, $P_{2N}/M_2^2\gamma$ exhibits a positive value between 70° and 110°, while it is negative at all other angles. At a 90° angle, $P_{2M}/M_2^2\gamma = 0$; for any other angle, it remains negative. The flow curvature gradient demonstrates a positive trend at obtuse shock angles $\theta > 118°$ and acute shock angles $\theta > 62°$, but is negative at other shock angles. The P_2 curve indicates an acceleration of the postshock streamline at acute shock angles $\theta > 75°$, with deceleration occurring for other acute angles. Furthermore, the trend of the pressure gradient in the $\boldsymbol{e_n}$ direction closely resembles that of P_2, making a significant contribution to the overall behaviour of P_2. For plotting purposes, after determining the Thomas curve, all the regions where P is ± 0.0001 are drawn. The variations in thickness of the Thomas curves is also due to this purpose.

Figure 4(*d*) shows the axisymmetric shock. The shock equation, given as

$$f = \frac{(x+6)^2}{9} - \frac{y^2}{9} - \frac{z^2}{9} - 1 = 0, \tag{3.14}$$

exhibits a shock angle of 90° at position $(-3, 0, 0)$. This is within the Cartesian (x, y, z)-space where the free stream velocity vector is aligned with the x-axis, i.e. the symmetry axis. The shock surface is hyperboloid, opening to the right with circular cross-sections. The shock shape of this example is the same as that shown in figure 5 of Emanuel &

https://doi.org/10.1017/jfm.2025.10859 Published online by Cambridge University Press

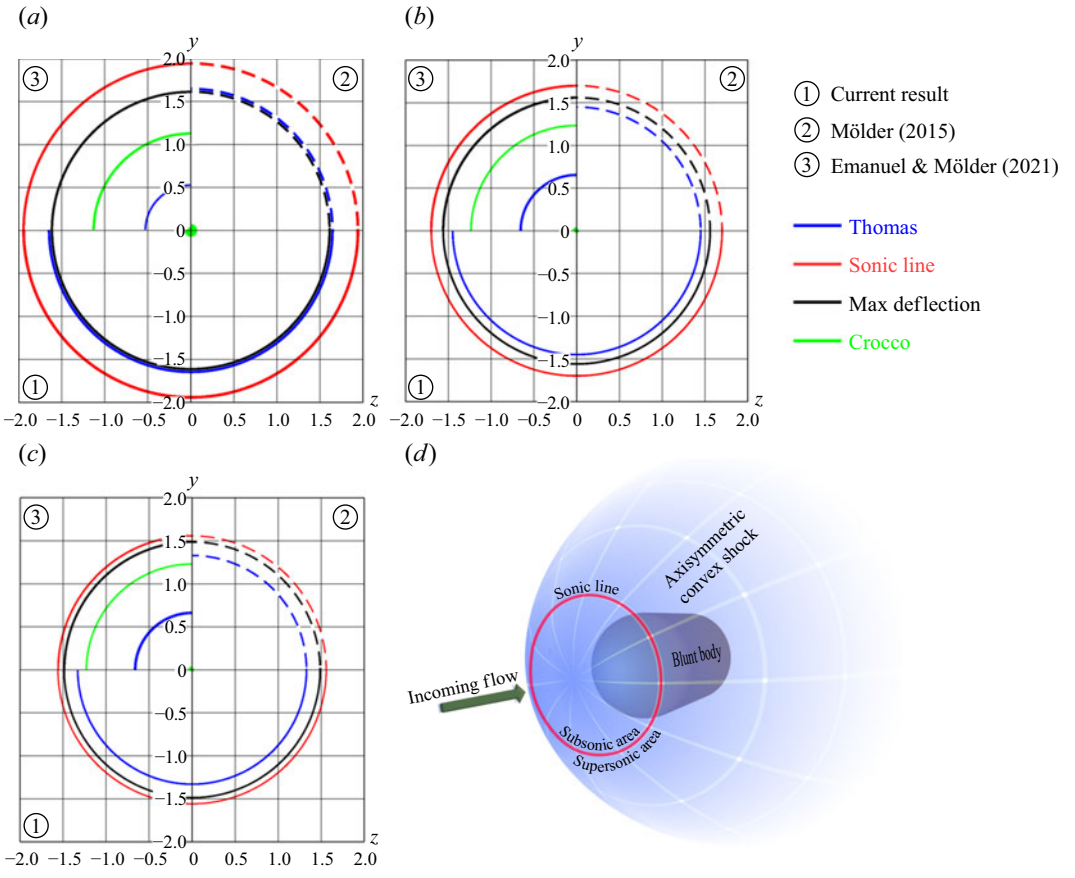


Figure 4. Special parameters at back of axisymmetric convex shock ($f = ((x+6)^2/9) - (y^2/9) - (z^2/9) - 1 = 0$). Here (*a*) $M_1 = 2$, (*b*) $M_1 = 3$, (*c*) $M_1 = 4$, (*d*) geometry of axisymmetric convex shock. The blue line is the Thomas point, the red line is the sonic line, the black line is the maximum deflection and the green line is the Crocco point.

Mölder (2021). In figure 4(*a–c*), ① represents the results obtained in this study, ② represents the results obtained using the theory of Mölder (2015) and ③ represents the results obtained in figures 5, 6 and 7 of Emanuel & Mölder (2021). A comparison indicates that the results of this study are consistent with those of Mölder (2015), but there is a significant difference from Emanuel & Mölder (2021). There are two primary reasons for the observed discrepancies. First, in Emanuel & Mölder (2021), the coordinate transformation equation used in deriving the 3-D curved shock governing equations contains restrictions. The transformation equation employed is (43) from Emanuel (2019). This equation is valid only for describing coordinate changes along two orthogonal principal curves on a surface. However, in Emanuel & Mölder (2021), the two orthogonal curves on the defined shock surface are not principal curves of the surface. Second, in Emanuel & Mölder (2021), one term describing surface curvature (denoted as (66) in Emanuel & Mölder (2021)) is directly defined as zero. This term, however, is non-zero in the case of concave or convex shocks. The 3D-CST-boos proposed in this paper can be well verified by the theory presented in Mölder (2015) in the axisymmetric case. This demonstrates the accuracy of 3D-CST-boos in solving the axisymmetric convex shock problem considered in this paper. In figure 4(*a–c*), the supersonic zone extends beyond the

https://doi.org/10.1017/jfm.2025.10859 Published online by Cambridge University Press

red line, while the subsonic zone is confined within it, encompassing the distribution of special parameters. The uniform incoming flow and the axisymmetric nature of the shock induce circular patterns in the postshock special parameter contours. The shape of the shock remains consistent because it is assumed to be the same shape. An increase in the incoming Mach number results in an enlargement of the wedge angle and the orthographic area of the object surface. Simultaneously, the subsonic area gradually diminishes, causing the maximum deflection position and the Thomas point to approach the axis. The Crocco point appears only on the axis. Further comprehensive analysis is now conducted. The sonic line and the maximum deflection position rely on zero-order flow parameters, which can be directly examined using the Rankine–Hugoniot equations. The Thomas and Crocco points are directly related to the first-order pressure parameters of (2.35), (2.36) and (2.44). For a fixed shock angle, increasing the Mach number does not alter the preshock pressure gradient, but intensifies the velocity gradient in the preshock region. Moreover, the coefficients preceding the pressure gradient and velocity gradient in (2.35), (2.36) and (2.44) increase with the rising Mach number, amplifying the pressure gradient of the downstream shock. As a result, the Thomas point moves towards the region of greater shock angle. This explains the observed phenomenon of Thomas points approaching the axis as the incoming Mach number increases.

4. Application of 3D-CST-boos

In practical supersonic flows, the incoming flow can be complex, featuring predominantly non-axisymmetric 3-D shocks. This section extends the application of 3D-CST-boos to analysis of the fundamental postshock parameter distribution in the presence of a non-uniform incoming flow. The theory is employed also to examine the special parameter distribution that occurs in more intricate shocks. All examples in this section depend on the geometric attributes of the shocks. Therefore, the discussion does not delve into the physical existence of shocks.The shock of each subsection is consistent. Assuming constant shock and changing incoming flow can better reflect the inverse design idea based on shock. Based on this idea, variant aircraft will become the focus of researches (Zhen 2022, Zhang 2024, Chen 2024). When the aircraft is flying, people want its performance to be as stable as possible, under different working conditions (Li 2018). By changing the shape of the aircraft during flight, it is possible to maintain performance by holding the shock and improve the operating range of the aircraft. For this purpose, This paper considers the postshock parameter distribution under different Mach numbers and angles of attack, which can provide theoretical help for related research.

4.1. *Three-dimensional elliptical convex shock*

4.1.1. *Uniform flow with AOA* $= 0°$

In figure 5, the shock equation is expressed as

$$f = \frac{(x+6)^2}{9} - \frac{y^2}{2.8^2} - \frac{z^2}{3.2^2} - 1 = 0, \tag{4.1}$$

with a shock angle of 90° at the position $(-3, 0, 0)$. The shock is symmetric about the $y = 0$ and $z = 0$ planes. Previous study (Zheng 2020*b*) has shown that the streamline behind the shock in the symmetric position does not exhibit lateral movement, whereas the streamlines in asymmetric positions exhibit significant lateral shift. Figure 5(*a–c*) illustrate the distinct parameter distributions of the shock surface at Mach numbers of 2, 3 and 4. For this illustration, the incoming flow parameters were set to $\gamma = 1.4$, $p_1 = \rho_1 = 1$. The shock shape adopts an elliptical form, and both the sonic line and the maximum deflection

https://doi.org/10.1017/jfm.2025.10859 Published online by Cambridge University Press

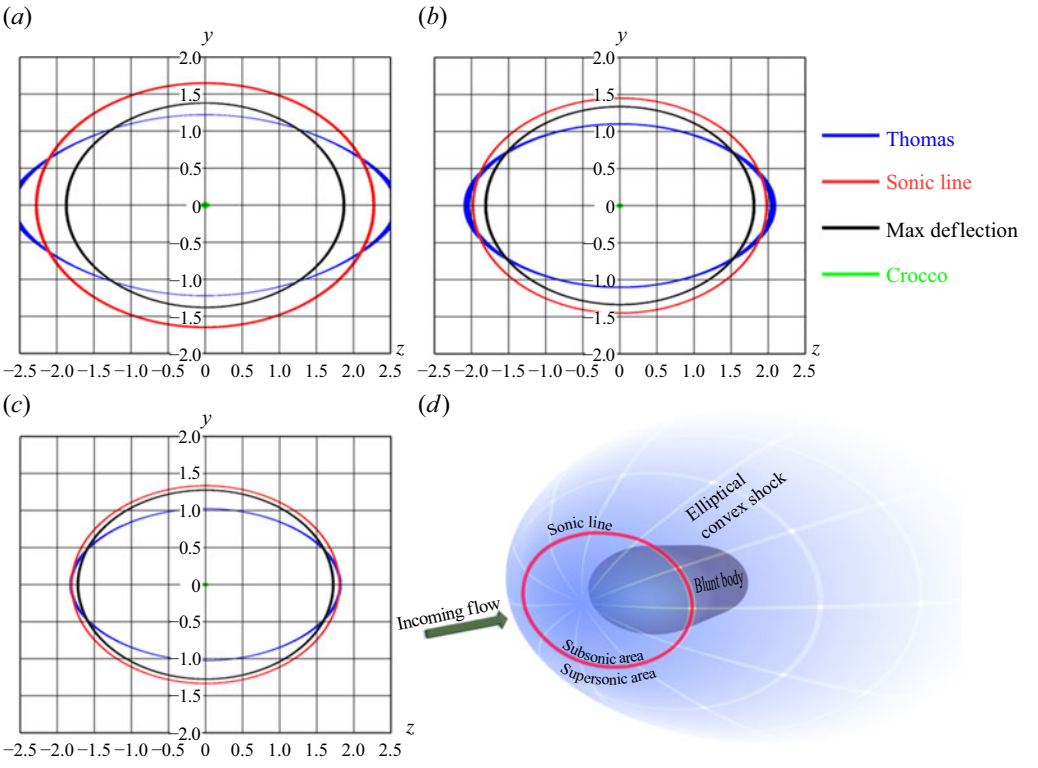


Figure 5. Special parameters at back of elliptical convex shock ($f = ((x+6)^2/9) - (y^2/2.8^2) - (z^2/3.2^2) - 1 = 0$). Here (*a*) $M_1 = 2$, (*b*) $M_1 = 3$, (*c*) $M_1 = 4$, (*d*) geometry of elliptical convex shock.

line of the postshock region take on elliptical shapes. The Thomas line displays a flatter ellipse intersecting the sonic line and the maximum deflection line. The Crocco points exclusively appear at the axis. With an increasing incoming Mach number, the subsonic area gradually diminishes, bringing the maximum deflection position closer to the axis. Simultaneously, the Thomas point approaches the central axis, causing the ratio of length-diameter to short-diameter of the Thomas line to decrease gradually, with the Thomas point in the z-direction moving closer to the axis at an accelerated rate. The Crocco points, however, remain unchanged.

Figure 6 presents the variations in the postshock gradient parameters along the $z = 0$ and $z = y$ planes. The green line depicts the streamline curvature, the blue line represents the pressure gradient along the streamline, the red line illustrates the change in $\partial p_2/\partial m$, the yellow line demonstrates the change in $\partial p_2/\partial n$ and the cyan line indicates the change in $\partial p_2/\partial l$. The position at which $\pi = 0$ is the Thomas point, and the location of $\kappa = 0$ is the Crocco point. The solid and dashed lines signify the first-order flow parameters in the $z = 0$ and $z = y$ planes, respectively. The streamline curvature κ initially increases from the starting point, reaching a maximum before decreasing to a minimum. The pressure gradient along the streamline, π, rapidly decreases from its maximum at the starting point to a minimum, remaining almost constant thereafter. The values of $\partial p_2/\partial n$ show a similar trend to π. This similarity arises from the small angle between the pressure gradient in the $\boldsymbol{e_n}$ direction, $\partial p_2/\partial n$, and the pressure gradient in the streamline direction, π. Most of the π value comes from the projection of $\partial p_2/\partial n$. At the starting position, $\partial p_2/\partial n$ and π have equivalent values, with the pressure gradient perpendicular to the streamline

https://doi.org/10.1017/jfm.2025.10859 Published online by Cambridge University Press

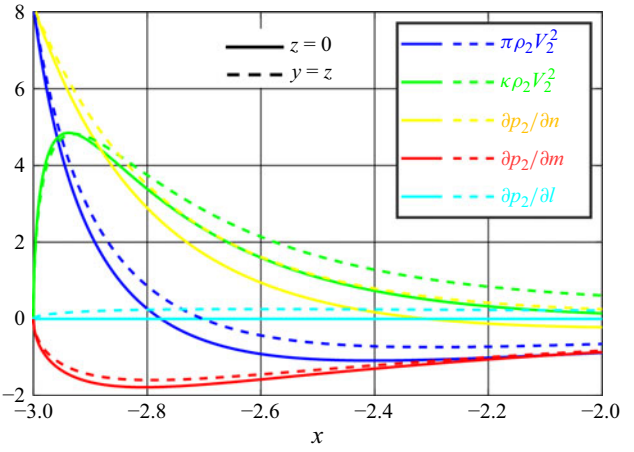


Figure 6. Variation of gradient parameters at the back of the elliptical convex shock ($f = ((x+6)^2/9) - (y^2/2.8^2) - (z^2/3.2^2) - 1 = 0$) at Mach 3. The solid line represents the $y = 0$ plane, the dashed line shows the $y = z$ plane. Different colours indicate pressure gradients in different directions.

being zero due to the 90° shock angle, indicating a normal shock. The value of $\partial p_2/\partial m$ decreases from a maximum at the starting point to a minimum, followed by a slow increase. In the $z = 0$ plane, $\partial p_2/\partial l$ is consistently equal to zero. However, in the $y = z$ plane, $\partial p_2/\partial l$ initially increases and then stabilizes. This discrepancy arises because the $z = 0$ plane perfectly aligns with the flow plane, and the $\boldsymbol{e_n}$ direction consistently lies within the $z = 0$ plane. On the contrary, the $y = z$ plane does not align with the flow plane. At the shock vertex $(-3, 0, 0)$, the $\boldsymbol{e_n}$ direction lies in the $y = z$ plane, while at other positions in the $y = z$ plane, the $\boldsymbol{e_n}$ direction forms an angle with the $y = z$ plane. Equation (2.35) illustrates that the pressure gradient in the postshock direction $\boldsymbol{e_l}$ is linked to the pressure, velocity and density gradients in the preshock direction $\boldsymbol{e_l}$. This observation emphasizes the inevitability of transverse pressure gradients in the flow field behind an asymmetric shock. These gradients serve as the fundamental basis for calculation errors in the flow field when the transverse flow is not considered.

4.1.2. *Uniform flow with angle of attack*

In figure 7, the shock equation is represented by

$$f = \frac{(x+6)^2}{9} - \frac{y^2}{2.8^2} - \frac{z^2}{3.2^2} - 1 = 0. \tag{4.2}$$

Figure 7 presents the distribution of special parameters behind an elliptical convex shock at an incoming Mach number of 4 with $AOA = 0°$, 5° and 10°. As the AOA increases, the special parameters obviously move in the negative direction of the y-axis. The subsonic area below the $z = 0$ plane gradually expands, and the y coordinate of the maximum deflection decreases. From the initial elliptical shape, the Thomas line gradually shifts in the negative direction of the y-axis and presents an asymmetric curve at $AOA = 10°$. Additionally, the top of the Thomas curve gradually narrows while the bottom widens. The Crocco point is deflected downward, and a second Crocco point appears in the fixed shock domain; this second Crocco point is also deflected downward as the AOA increases. The Crocco points appear only in the $z = 0$ plane, mainly because the $z = 0$ plane coincides with the flow plane, and $\partial p_2/\partial l$ is always zero. Analysing the Crocco points across the entire shock surface using (2.35), (2.36) and (2.44) is complex due to the lack of a

https://doi.org/10.1017/jfm.2025.10859 Published online by Cambridge University Press

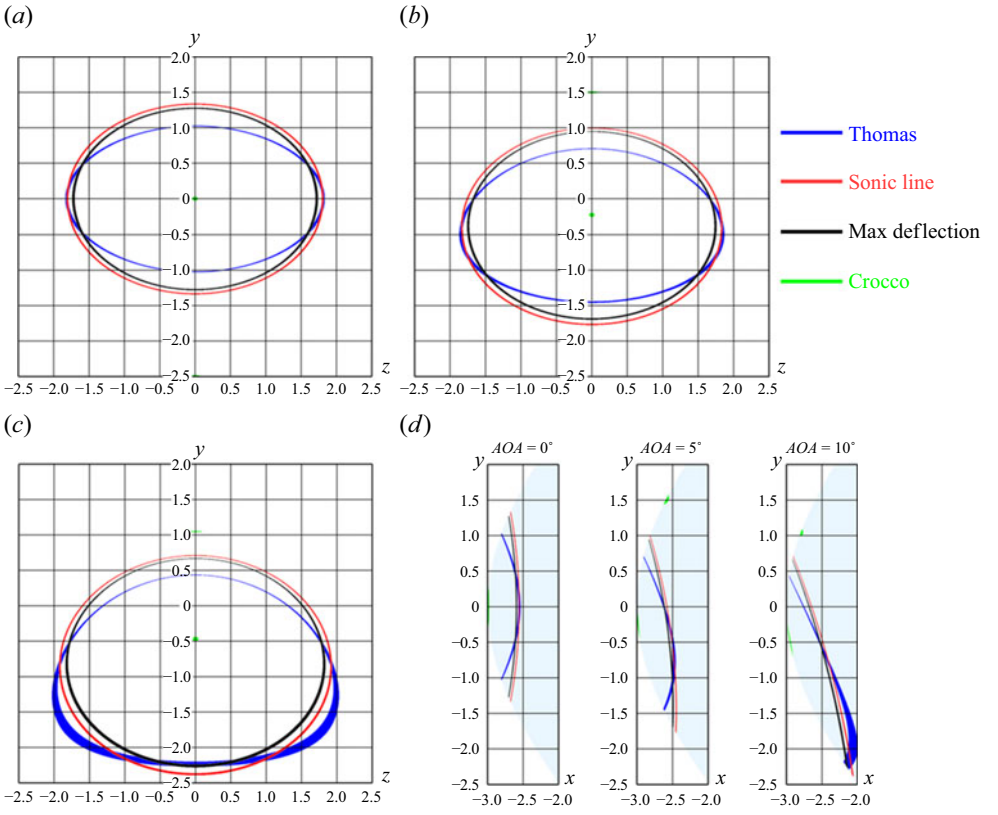


Figure 7. Special parameters at back of elliptical convex shock ($f = ((x+6)^2/9) - (y^2/2.8^2) - (z^2/3.2^2) - 1 = 0$) at Mach 4. Here (*a*) $AOA = 0°$, (*b*) $AOA = 5°$, (*c*) $AOA = 10°$, (*d*) side view.

consistent relationship between the *AOA* and the velocity gradient of the preshock region. This is different from the relationship with the Mach number, where an increase in the Mach number results in a direct increase in the velocity gradient of the preshock region across the entire shock surface. Focusing on a specific point, such as the central Crocco point, makes it easier to analyse the effect of changes in the *AOA* on that location. As the *AOA* increases, the shock angle decreases, so $\partial p_2/\partial m$ is no longer zero. This results in a component perpendicular to the streamline. Additionally, π is no longer zero, so the streamline at this point will be deflected, and the Crocco point will disappear. Figure 7(*d*) shows a side view of the distribution of the special parameters as the *AOA* changes. With an increase in the *AOA*, the special parameters indicate a deflection of the flow direction. Generating such a shock under such incoming flow conditions requires more complex and stringent physical surface conditions.

4.1.3. *Non-uniform flow*

Non-uniformity in the incoming flow greatly affects the parameters of each order behind the shock. Indeed, the flow field preceding a reflected shock is often characterized by non-uniformity. The 3D-CST-boos formulation is valuable in investigating the first-order flow parameters following shocks in non-uniform incoming flows. Figure 8 shows the special parameter distributions behind an elliptical convex shock for a non-uniform incoming flow. The incoming flow pressure equations are even functions in all four cases illustrated in figure 8. The pressure distribution of the incoming flow is directly specified via the

https://doi.org/10.1017/jfm.2025.10859 Published online by Cambridge University Press

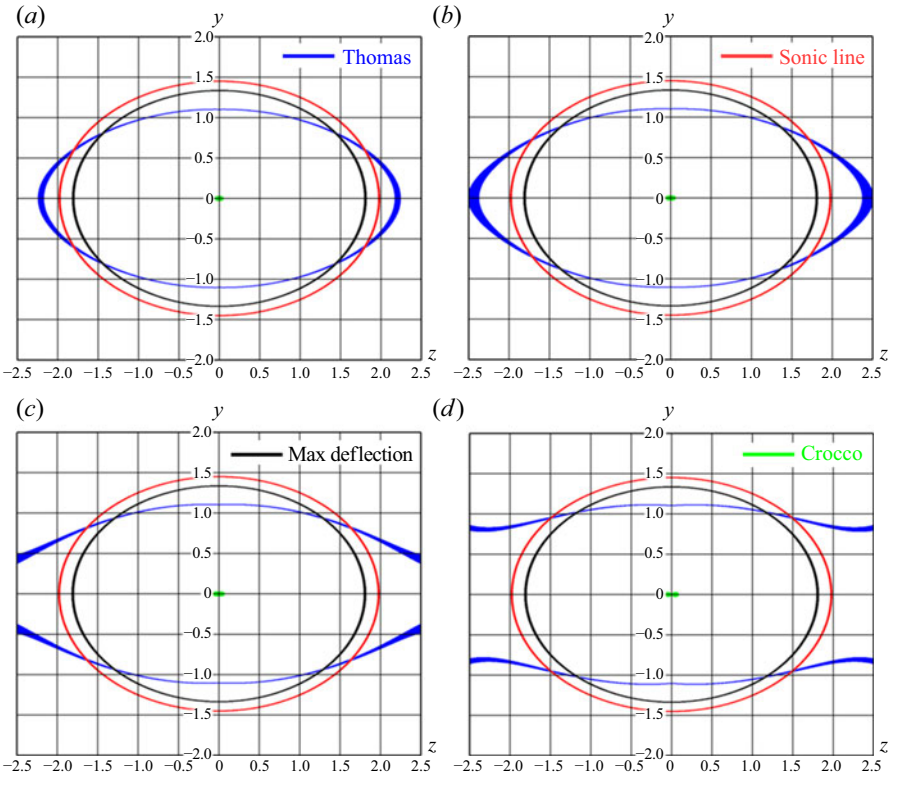


Figure 8. Special parameters at back of elliptical convex shock $(f = ((x+6)^2/9) - (y^2/2.8^2) - (z^2/3.2^2) - 1 = 0)$ at Mach 3. Here (a) $p1 = 0.01|z| + 1$, (b) $p1 = 0.02|z| + 1$, (c) $p1 = 0.03|z| + 1$, (d) $p1 = 0.05|z| + 1$.

various equations. This enables a more direct study of the influence of non-uniformity in the incoming flow on the flow parameters behind the shock. As can be seen from figure 8, the zero-order physical parameters (sonic line and maximum deflection) have an oval shape that does not change with the pressure function. This phenomenon is well understood, because the postshock Mach number is related only to the preshock Mach number and the shock angle. That is, the postshock Mach number is independent of the incoming pressure. Similarly, the postshock deflection angle is only related to the preshock Mach number and the shock angle, and is independent of the incoming pressure. However, the first-order flow parameters are greatly affected by the preshock incoming pressure. In figure 8, the position of the Crocco point does not change, but the Thomas point shifts dramatically. As the coefficient of the incoming pressure function z gradually increases, the Thomas point moves to the positive and negative semiaxis of z until the curve is no longer continuous and finally divides into two parts. The Thomas point in the $z = 0$ plane does not change, because the pressure at $z = 0$ does not vary.

Figure 9 shows the distribution of first-order flow parameters in the $y = 0$ plane. The solid line represents the case where the incoming flow pressure is $p1 = 0.01|z| + 1$, and the dashed line represents the case where the incoming flow pressure is $p1 = 0.05|z| + 1$. The other two pressure distributions fall somewhere inbetween and are no longer analysed. The pressure gradient along the streamline (π) shows a downward trend from the maximum value, while the curvature of the streamline (κ) increases from zero to the maximum value, and then gradually decreases. When $\pi = 0$, the Thomas point appears,

https://doi.org/10.1017/jfm.2025.10859 Published online by Cambridge University Press

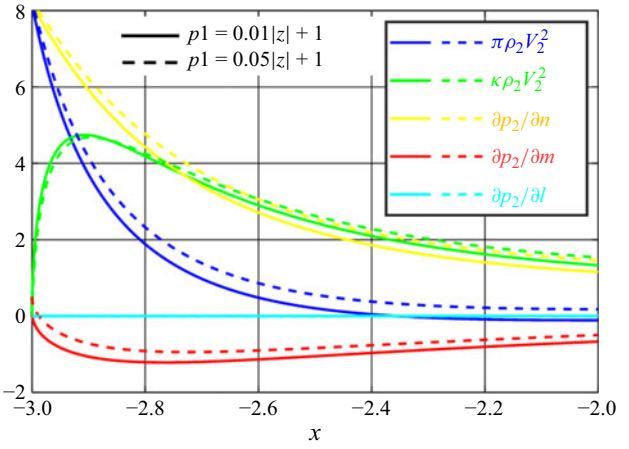


Figure 9. Variation of gradient parameters at the back of the elliptical convex shock ($f = ((x+6)^2/9) - (y^2/2.8^2) - (z^2/3.2^2) - 1 = 0$) at Mach 3. The solid line indicates that the incoming flow pressure function is $p1 = 0.01|z| + 1$, and the dashed line indicates that the incoming flow pressure function is $p1 = 0.05|z| + 1$.

and when $\kappa = 0$, the Crocco point appears. It is clear that $\partial p_2/\partial m$ decreases from zero to a minimum and then slowly increases. The change trend of $\partial p_2/\partial n$ is basically the same as that of π, mainly because the angle between the two gradient vectors is small. The value of $\partial p_2/\partial l$ is always zero, and the flow plane coincides exactly with the $y = 0$ plane. For the three gradient values of $\partial p_2/\partial l$, $\partial p_2/\partial m$ and $\partial p_2/\partial n$, the dashed line is always above the solid line. When the incoming Mach number and shock shape are unchanged, the preshock velocity gradient does not change, and the coefficients in (2.35), (2.36) and (2.44) remain the same. As the pressure function coefficient increases, the preshock pressure gradient in the three directions becomes larger, and finally the postshock pressure gradient increases. However, π and κ do not follow these change laws. This is because π and κ are projected by $\partial p_2/\partial l$, $\partial p_2/\partial m$ and $\partial p_2/\partial n$, and their magnitudes depend not only on the values of $\partial p_2/\partial l$, $\partial p_2/\partial m$ and $\partial p_2/\partial n$, but also on the angle relationship.

4.2. *Three-dimensional elliptical concave shock*

The core content of this subsection has three parts. First, using 3D-CST-boos to solve the first-order parameter behind elliptical/axisymmetric concave shocks. Second, the first-order parameters are used to explain the reasons for the difference in flow field (elliptical/axisymmetric internal flow). Thirdly, the correctness of 3D-CST-boos in 3-D curved shocks is verified.

Elliptical concave shocks find practical applications in aircraft design, serving as an optimal choice for realizing the inverse design of waveriders and 3-D internal turning inlets. Additionally, these shocks are frequently observed in the inlets of traditional fighter jets. Accurate calculation of first-order parameters following an elliptical concave shock is crucial for comprehending the postshock flow field. Figure 10(*a*) presents a 3-D geometric diagram of an elliptical concave shock. The colour of the shock surface signifies the progressive intensification of the shock. In an ideal scenario, the elliptical concave shock would approach infinite convergence at the axis. However, in most cases, the convergence of the concave shock is preceded by a complex Mach reflection phenomenon, as demonstrated in a recent study by Zhang (2023*a*). At the intersection of the incident shock and Mach stem, the curvature of the 3-D curved shock becomes discontinuous, rendering 3D-CST-boos inapplicable. This section centres on analysing the ideal scenario

https://doi.org/10.1017/jfm.2025.10859 Published online by Cambridge University Press

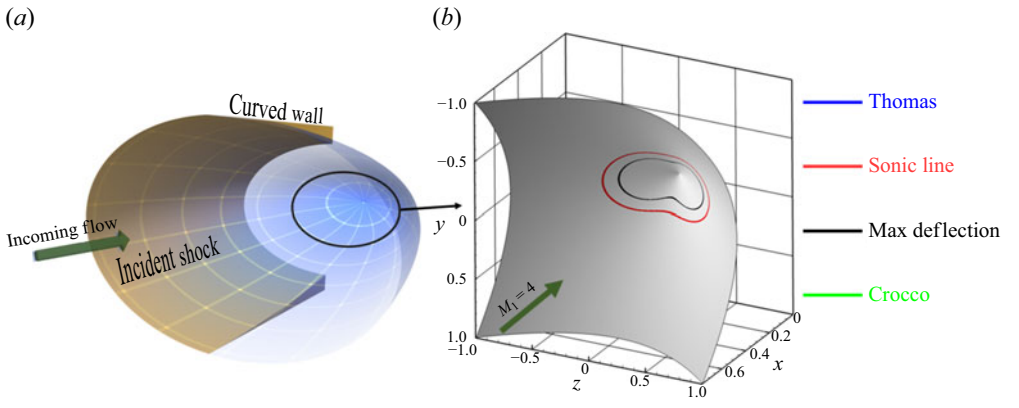


Figure 10. Special parameters at back of an elliptical concave shock ($f = e^{\sqrt{(y^2/2.4^2)+(z^2/2.8^2)}} - 1 - x = 0$) at Mach 4. The solid line represents the $y = 0$ plane. The dashed line shows the $z = 0$ plane.

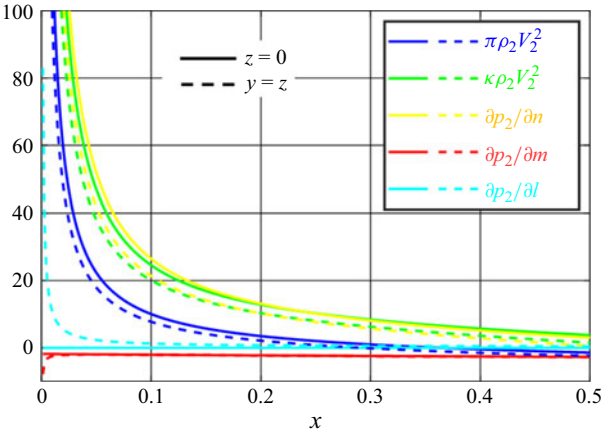


Figure 11. Variation of gradient parameters at the back of an elliptical concave shock ($f = e^{\sqrt{(y^2/2.4^2)+(z^2/2.8^2)}} - 1 - x = 0$) at Mach 4. The solid line represents the $z = 0$ plane. The dashed line shows the $y = z$ plane.

of an elliptical concave shock, assuming indefinite convergence towards the axis with an $AOA = 90°$ shock angle at the axis. With an incoming flow at Mach 4, figure 10(*b*) illustrates the distribution of specific postshock parameters. The Thomas curve displays symmetry across the $y = 0$ plane, and is divided into upper and lower parts by this plane. Seen from the direction of the incoming flow, the sonic line and maximum deflection resemble two figures-of-eight. In real non-viscous flow, a more intricate 3-D Mach reflection phenomenon emerges within the region bounded by the sonic line. The Crocco point exclusively appears at the shock surface's vertex.

Figure 11 shows the first-order postshock parameter distribution of an elliptical concave shock given by

$$f = e^{\sqrt{\frac{y^2}{2.4^2}+\frac{z^2}{2.8^2}}} - 1 - x = 0 \tag{4.3}$$

at $z = 0$ and $y = z$. In the above two planes, the change trends of π, κ and $\partial p_2/\partial n$ are the same, decreasing rapidly from their maximum values and then slowly decaying.

https://doi.org/10.1017/jfm.2025.10859 Published online by Cambridge University Press

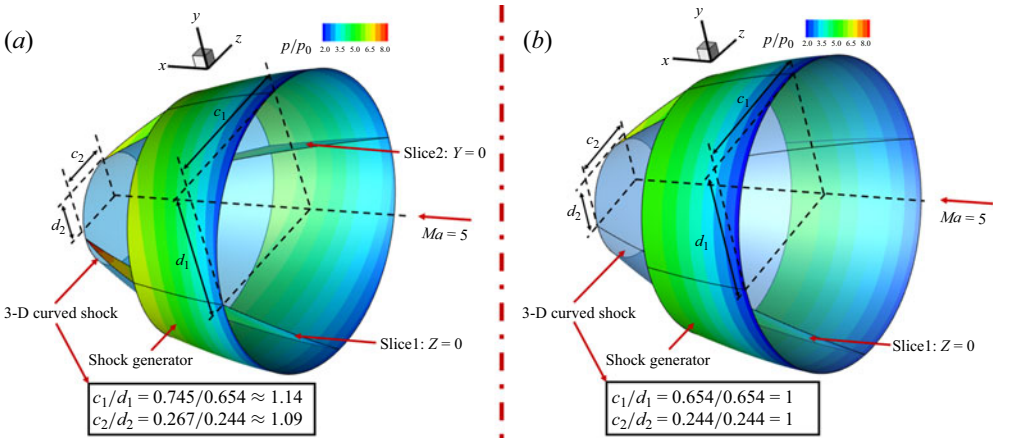


Figure 12. Pressure flow field behind an elliptical concave shock ($F = (z^2/(-0.17x^2 - 0.24x + 0.8)^2) + (y^2/(-0.15x^2 - 0.2x + 0.7)^2) - 1$) and an axisymmetric concave shock ($F = (z^2/(-0.15x^2 - 0.2x + 0.7)^2) + (y^2/(-0.15x^2 - 0.2x + 0.7)^2) - 1$).

Thomas points exist in these two planes, whereas Crocco points do not. In the $z = 0$ plane, $\partial p_2/\partial l$ is always zero and $\partial p_2/\partial m$ remains constant. In the $y = z$ plane, $\partial p_2/\partial l$ rapidly decreases from its maximum and eventually remains constant. In contrast, $\partial p_2/\partial m$ rapidly increases from its minimum and reaches a plateau. The absolute value of the postshock pressure gradient in all three directions in the $y = z$ plane is always higher than that in the $z = 0$ plane. It is difficult to analyse this phenomenon with (2.35), (2.36) and (2.44), mainly because the coefficients of these equations and the preshock velocity gradient are constantly changing.

In general, the exploration of 2-D axisymmetric shocks entails the characterization of shock shapes through quadratic or exponential functions. This section extends the analysis to quadratic 3-D concave shocks, particularly focusing on the impact of postshock flow parameters on the entire flow field. This influence directly affects the aerodynamic performance of internal turning inlets or waveriders based on the shock flow fields described above. For the 3-D elliptical concave shock shown in figure 12(*a*), the shock equation is

$$F = \frac{z^2}{\left(-0.17x^2 - 0.24x + 0.8\right)^2} + \frac{y^2}{\left(-0.15x^2 - 0.2x + 0.7\right)^2} - 1. \tag{4.4}$$

The long axis to short axis ratio at the front of the elliptical concave shock is 1.14, and the long axis to short axis ratio at the back of the elliptical concave shock is 1.09. The shock curvature κ_{nm} is constantly changing at any section along the direction of the incoming flow. The shock curvature κ_{nl} and κ_{gl} is also constantly changing at any cross-section perpendicular to the direction of the incoming flow. An axisymmetric concave shock is constructed using the short semiaxis of the elliptical concave shock, the equation for which is

$$F = \frac{z^2}{\left(-0.15x^2 - 0.2x + 0.7\right)^2} + \frac{y^2}{\left(-0.15x^2 - 0.2x + 0.7\right)^2} - 1. \tag{4.5}$$

The ratio of the long axis to the short axis of the axisymmetric concave shock is always one. The shock curvature κ_{nm} is constantly changing in any section along the direction of

https://doi.org/10.1017/jfm.2025.10859 Published online by Cambridge University Press

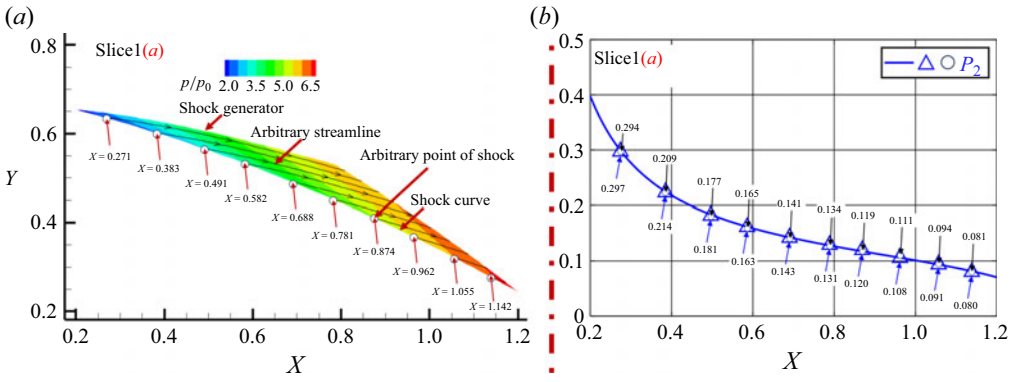


Figure 13. Verification of the 3-D curved shock theory. (*a*) Elliptical concave shock pressure distribution on the $z = 0$ plane. (*b*) Difference pressure gradient compared with the pressure gradient obtained from theory. Triangles represent the pressure gradient obtained from the 3-D curved shock theory, and circles represent the difference used to obtain the pressure gradient.

incoming flow. The shock curvature κ_{nl} and κ_{gl} is constant in any section perpendicular to the direction of incoming flow.

The LTOC (Zheng 2020*b*) is an inverse method to solve the 3-D supersonic flow field. It discretized the 3-D flow field into a series of 2-D flow planes, solved the flow field in the 2-D flow plane and reconstructed the whole 3-D flow field by coordinate transformation. The detailed process of using LTOC to solve 3-D flow field can be divided into three steps. First, the concept of a micro-osculating plane is used to disperse the given 3-D curved shock, and the shock curve in each flow plane is obtained. Then, each discrete shock line is rotated around the X-axis to the same virtual meridian plane, and the non-coaxial method of characteristics proposed in Zheng (2020*a*) is used to solve the problem. Finally, the 2-D flow field parameters obtained in the virtual meridian plane are converted to the 3-D Cartesian rectangular coordinate system. The complete 3-D flow behind the shock is formed by the combination of flows in these flow planes.

As shown in figures 12(*a*) and 12(*b*), when the incoming Mach number is 5 and the incoming flow height is at 17 km, the LTOC of Zheng (2020*b*) can be used to inversely design the flow field behind two different shocks. The accuracy of the above inverse design method has been verified by Zheng (2020*b*), in which the flow field and the wall are inverted based on 3-D shocks to within an accuracy of 3 %. By comparing the flow field generated by two different shocks in figure 12, it can be found that the uneven transverse curvature of the elliptical concave shock leads to a relatively obvious transverse pressure gradient in the asymmetric position. Thus, the isobaric pressure line is not oval. However, the transverse curvature generated by the axisymmetric concave shock is uniform and there is no transverse pressure gradient. As a result, the isobaric line is obviously circular. The pressure increases more rapidly along the long axis of the elliptical concave shock than along the short axis. The pressure of the axisymmetric concave shock increases at the same rate along both axes.

Slice1(a) in figure 12(*a*) is selected to verify the correctness of the higher-order parameters obtained by solving the 3D-CST-boos governing equations. The main reason for choosing this surface is that the flow plane here is completely coincident with slice1, and the postshock streamline is completely bounded in slice1, making it easy to extract the streamline. As shown in figure 13(*a*), 10 streamlines were extracted and the pressure parameters on the streamline near the shock point were obtained. The pressure gradient π of any shock point along the streamline can be obtained using a difference method.

https://doi.org/10.1017/jfm.2025.10859 Published online by Cambridge University Press

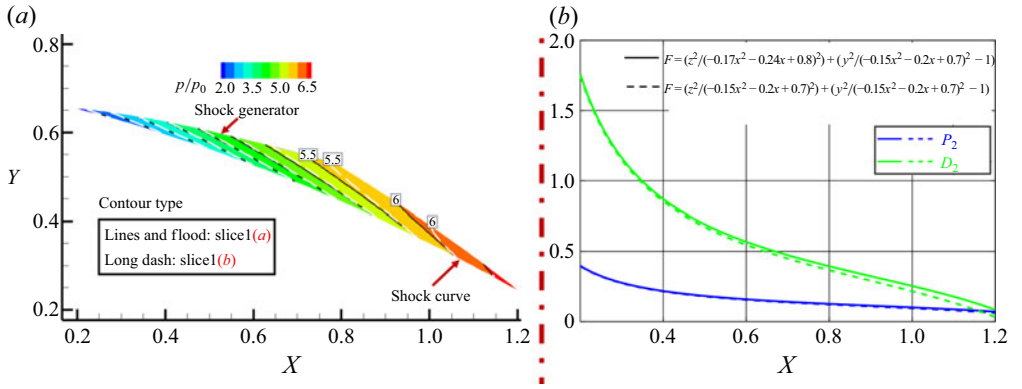


Figure 14. (*a*) Comparison of flow field between elliptical concave shock and axisymmetric concave shock at $z=0$ plane. (*b*) Pressure gradients at $z=0$ plane; the solid line is the elliptical concave shock and the dashed line is the axisymmetric concave shock.

Here (2.35), (2.36) and (2.44) were employed to directly compute the first-order pressure parameter distribution of the corresponding shock points. Here (2.47) was used to derive the pressure gradient along the streamline, as illustrated in figure 13(*b*). In this figure, the blue line depicts the pressure distribution along the postshock streamline of slice1 obtained using 3D-CST-boos. The triangles correspond to the actual value of the pressure gradient of the selected shock point in figure 13(*a*), while the circles represent the approximation obtained by the difference method. Statistical analysis reveals that the maximum difference in the first-order physical property parameters is less than 3 %. This discrepancy primarily stems from iterative errors within the LTOC method during the flow field calculations.

In figure 14(*a*), the $z=0$ planes from figures 12(*a*) and 12(*b*) are selected for further analysis. 'Lines and flood' represents the pressure distribution of the $z=0$ plane in figure 12(*a*) and 'long dash' represents the pressure distribution of the $z=0$ plane in figure 12(*b*). On the $z=0$ plane, the elliptical concave shock shape and the axisymmetric concave shock shape are the same. Macroscopically, the two pressure clouds at $z=0$ are roughly the same. However, at the rear of the flow field, the pressure of the flow field generated by the elliptical concave shock increases more obviously. Additionally, the equal pressure line of the flow field generated by the elliptical concave shock obviously appears earlier than that of the flow field generated by the axisymmetric concave shock. On the $z=0$ plane, the elliptical and axisymmetric concave shock shapes are given by

$$F=\frac{y^2}{\left(-0.15x^2-0.2x+0.7\right)^2}-1, \tag{4.6}$$

but there is no theoretical explanation for the difference in pressure growth behind the shock. However, the reason can be explained by the 3D-CST-boos proposed in this paper. As shown in figure 14(*b*), the theory gives the first-order postshock flow parameters at the $z=0$ position. The solid line represents the elliptical concave shock and the dashed line represents the axisymmetric concave shock. Figure 14(*b*) shows that the first-order flow parameters behind the elliptical concave shock are slightly higher than those behind the axisymmetric concave shock. This is because the elliptical concave shock curvature κ_{nl} and κ_{gl} is not uniform in the transverse position. Higher values of the first-order postshock flow parameters κ and π correspond to faster pressure growth along the streamline. This is why the elliptical concave shock pressure increases faster in figure 14(*a*). This conclusion will better guide the design of waveriders. When a waverider with higher compression

https://doi.org/10.1017/jfm.2025.10859 Published online by Cambridge University Press

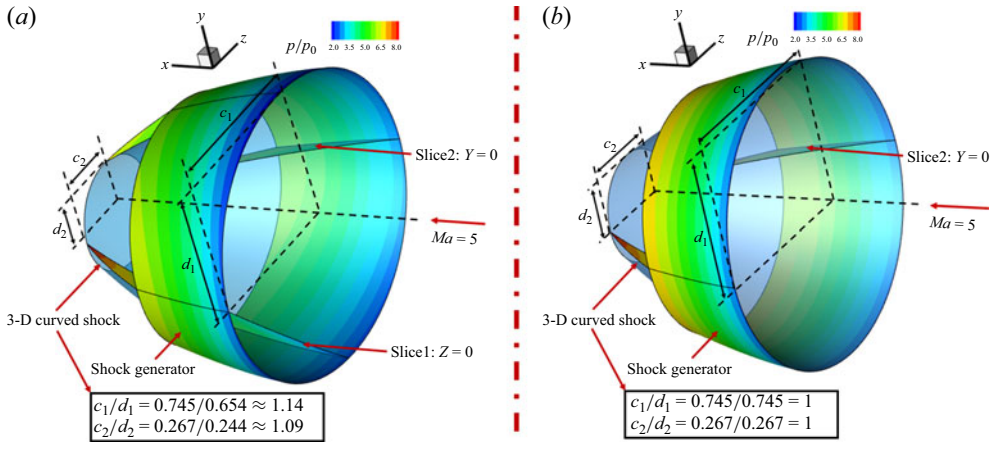


Figure 15. Pressure flow field behind an elliptical concave shock ($F = (z^2/(-0.17x^2 - 0.24x + 0.8)^2) + (y^2/(-0.15x^2 - 0.2x + 0.7)^2) - 1$) and an axisymmetric concave shock ($F = (z^2/(-0.17x^2 - 0.24x + 0.8)^2) + (y^2/(-0.17x^2 - 0.24x + 0.8)^2) - 1$).

efficiency is required, the elliptical concave shock can be used for inverse design. When a waverider with smaller transverse flow is needed, the axisymmetric concave shock can be used. For inlet design, the inverse pressure gradient in the inlet separation area determines the separation scale. If the 3-D shock can be reasonably organized so that the pressure gradient behind the shock can be effectively controlled, it is effective for reducing flow separation.

A new axisymmetric concave shock is constructed using the long semiaxis of the elliptical concave shock, the shock equation for which is

$$F = \frac{z^2}{\left(-0.17x^2 - 0.24x + 0.8\right)^2} + \frac{y^2}{\left(-0.17x^2 - 0.24x + 0.8\right)^2} - 1. \tag{4.7}$$

The 3-D postshock flow field structure is shown in figure 15(*b*). As can be seen from figure 15(*a*), the pressure growth rate at the position of the long semiaxis ($y = 0$) of the elliptical concave shock is significantly higher than that at the position of the short semiaxis ($z = 0$). This is mainly because the pressure growth rate at the positions of the long and short semiaxes is strongly related to the curvature κ_{nl} and κ_{gl}. For the same x-coordinate, the curvature at the long semiaxis is significantly greater than that at the short semiaxis. In addition, the postshock pressure gradient of the long semiaxis is significantly greater than that of the short semiaxis. Therefore, the pressure growth rate of the $y = 0$ plane flow field is higher than that of the $z = 0$ plane flow field. By comparing the 3-D flow fields based on the axisymmetric shock and the elliptical shock, the isopressure line of the former is obviously circular along the direction of the incoming flow, while the latter does not have such a structure.

Similarly, slice2 in figure 15(*a*) can be used to verify the correctness of the 3D-CST-boos proposed in this paper. Eleven streamlines were extracted at arbitrary shock positions in slice2, as shown in figure 16(*a*), and the pressure gradient difference near the shock was obtained. The postshock pressure gradient along the streamline at slice2 is given by 3D-CST-boos, resulting in the blue curve in figure 16(*b*). A comparison indicates that 3D-CST-boos can accurately solve the pressure gradient in any postshock direction.

Figure 17(*a*) shows the $y = 0$ planes in figures 15(*a*) and 15(*b*) for further analysis. 'Flood' represents the pressure distribution of the $y = 0$ plane in figure 15(*a*) and

https://doi.org/10.1017/jfm.2025.10859 Published online by Cambridge University Press

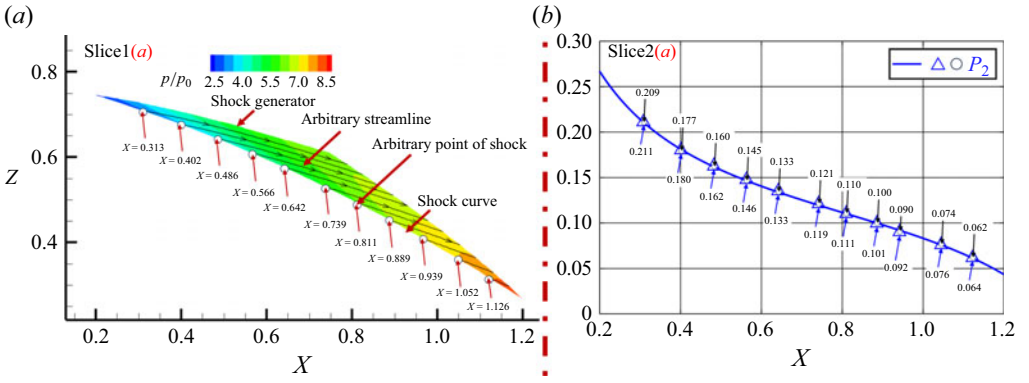


Figure 16. Verification of the 3-D curved shock theory. (*a*) Elliptical concave shock pressure distribution on the $y = 0$ plane. (*b*) Difference pressure gradient compared with the pressure gradient obtained from theory. The triangles represent the pressure gradient obtained from the 3-D curved shock theory and the circles represent the difference used to obtain the pressure gradient.

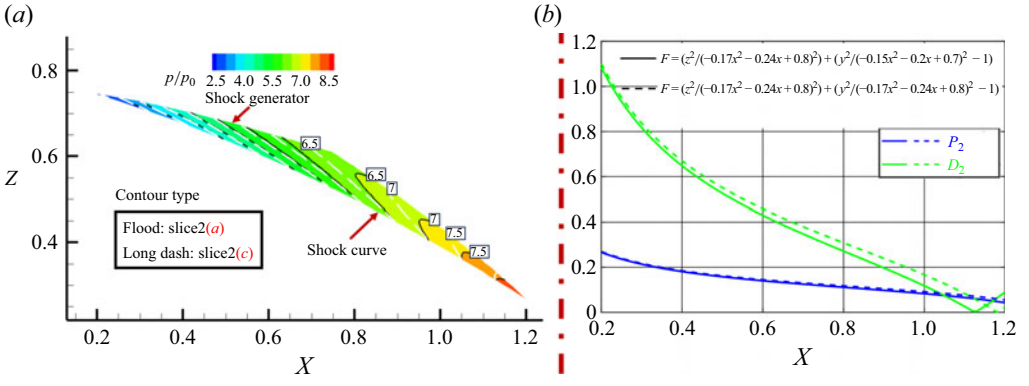


Figure 17. (*a*) Comparison of flow field between elliptical concave shock and axisymmetric concave shock at $y = 0$ plane. (*b*) Pressure gradients at $y = 0$ plane; the solid line is the elliptical concave shock and the dashed line is the axisymmetric concave shock.

'long dash' represents the pressure distribution of the $y = 0$ plane in figure 15(*b*). By comparison, it can be found that the pressure growth rate of the axisymmetric concave shock is significantly higher than that of the elliptical concave shock. This is different from the conclusion reached in figure 14(*a*). However, the 3D-CST-boos can still be used for the relevant analysis. The pressure gradient behind the two different shocks is shown in figure 17(*b*). The dashed line shows the result for the axisymmetric concave shock and the solid line shows the result for the elliptical concave shock. The dotted line is always above the solid line, demonstrating that, on $y = 0$, the pressure gradient behind the axisymmetric concave shock based on the long axis is higher than that behind the elliptical concave shock. Thus, the pressure along the streamline increases faster and the curve of the streamline is more obvious.

4.3. *Other special shocks*

For existing supersonic flight, vehicles with 3-D inward-turning hypersonic inlets are being extensively studied (You 2006; Zhang 2023*b*). The lower lip of such inlets is often V-shaped, as shown in figure 18(*a*). The global shock structure at the lower lip is often complicated, but the local shock generated by the V-shaped lip can be approximated as

https://doi.org/10.1017/jfm.2025.10859 Published online by Cambridge University Press

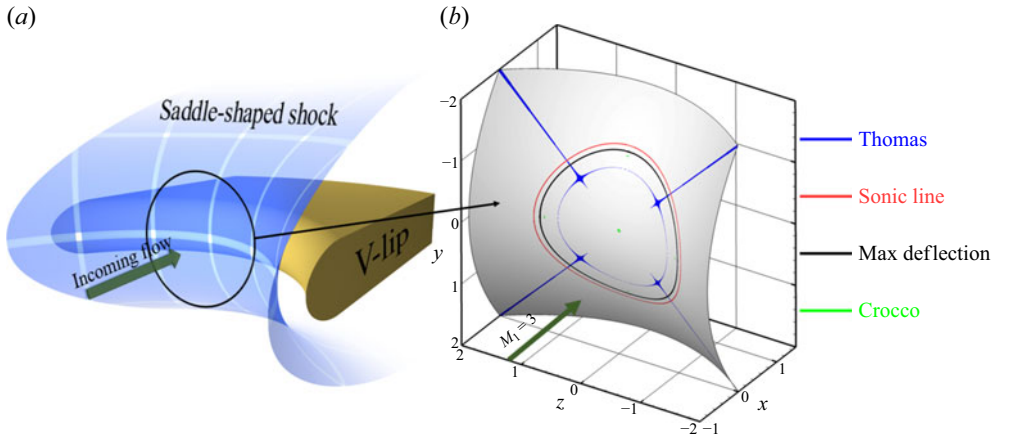


Figure 18. Special parameters at back of saddle-shaped shock ($f = x - (y^2/5) + (z^2/5) = 0$) at Mach 3.

a saddle-shaped shock. The flow condition behind this shock will affect the aerodynamic performance of the whole inlet. The proposed 3D-CST-boos can be used to analyse the flow condition behind the saddle-shaped shock. Figure 18(*b*) shows the postshock special parameter distribution when the Mach number of the flow is 3 and the shock shape is

$$f = x - \frac{y^2}{5} + \frac{z^2}{5} = 0. \tag{4.8}$$

A larger shock angle in the central region will produce an obvious subsonic zone. If facing along the incoming stream, its sonic line will be approximately circular. The maximum deflection line appears in the subsonic zone and is roughly the same shape as the sonic line. The Crocco points are discontinuous and scattered in the centre of the shock and the symmetric position of the shock. The Thomas line extends indefinitely outward from the centre point in the $x = y$ and $x = -y$ planes. Thomas points also occur in subsonic and supersonic regions.

The proposed 3D-CST-boos enables the temperature gradients near the V-shaped lip shocks to be calculated. This facilitates the identification of regions with high temperature gradients. The derivation of the temperature gradient is similar to that of the pressure gradient, and the final result is as follows:

$$T_{2l} = P_{2l} - R_{2l}, \tag{4.9}$$

$$T_{2m} = P_{2m} - R_{2m}, \tag{4.10}$$

$$T_{2n} = -V_{2m}/V_{2n}T_{2m} + (\gamma - 1)/\gamma V_{2m}/V_{2n}P_{2m} + (\gamma - 1)/\gamma P_{2n}. \tag{4.11}$$

Figure 19 illustrates the cloud diagram of temperature gradient distributions following saddle-shaped shock, computed directly from (4.9) to (4.11). Figure 19(*a–c*) detail the distributions of temperature gradients in the l, m and n directions, respectively. Due to the uniform incoming flow without angle of attack and the symmetric nature of the shock function, the absolute values of the temperature gradient distributions postshock are symmetric about the $z = 0$ and $y = 0$ planes. It is value to note that the l and m directions on either side of this symmetric position on the shock surface are opposite, resulting in differences in the signs of the temperature gradients. At the origin of the shock, the temperature gradients in all three directions are zero, where the temperature is at its maximum and the gradient at its minimum. The $z = 0$ and $y = 0$ planes coincide with the postshock flow plane at this position, maintaining a zero-temperature gradient in the

https://doi.org/10.1017/jfm.2025.10859 Published online by Cambridge University Press

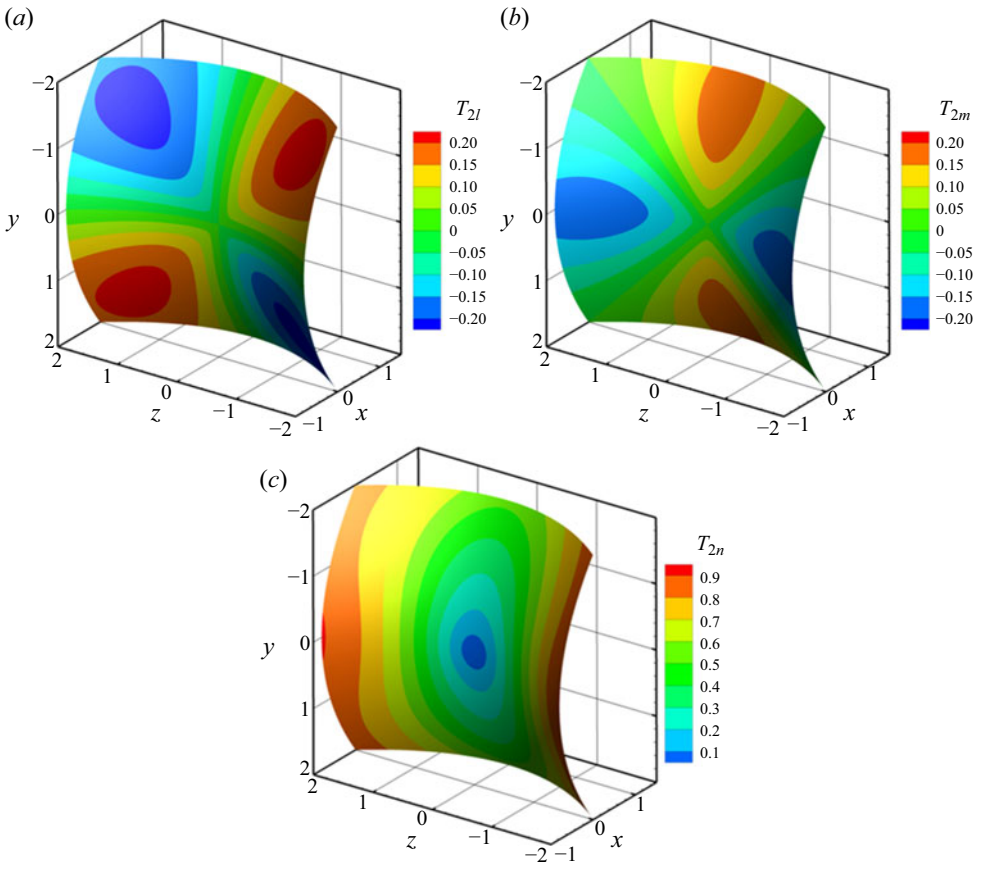


Figure 19. Temperature gradient distribution behind saddle-shaped shock.

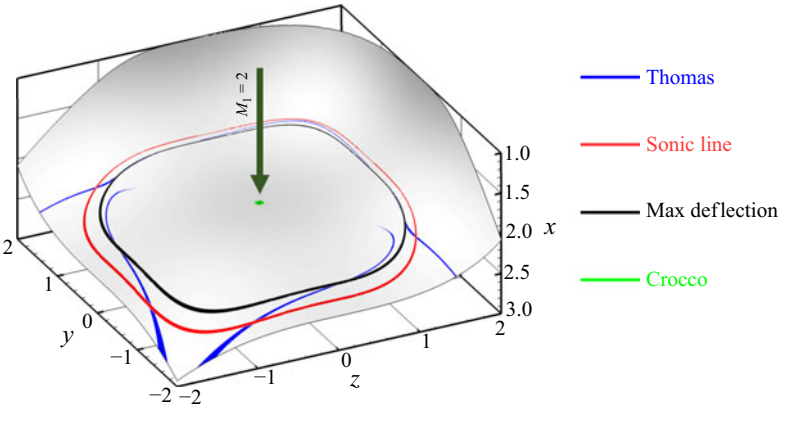


Figure 20. Special conditions at back of cubic surface shock ($f = (x^3/9) + (y^3/9) + (z^3/9) - 1 = 0$) at Mach 2.

l direction, while the gradients in the m and n directions progressively increase from the centre towards the edges. The present paper provides a theoretical foundation for the study of temperature gradients distribution characteristics behind saddle-shaped shock.

Figure 20 shows the distribution of special parameter curves behind a cubic surface shock. As the normal vector of the cubic surface is no longer a linear equation, the special

https://doi.org/10.1017/jfm.2025.10859 Published online by Cambridge University Press

parameter curves under the cubic surface become more complex. Although the given surface function is relatively regular, the actual surface and special parameter distribution do not exhibit obvious regularity. Hence, a higher-order equation may be needed to describe these changes.

5. Conclusions

This paper has introduced the derivation of 3D-CST-boos equations within a orthogonal frame field of the shock surface. A direct connection between the shock curvature and the flow parameter gradients was established. In practical applications, the advantages of employing this succinct 3D-CST-boos are apparent, as the theory is no longer constrained to specific shock shapes or incoming flow conditions.

Removing the $\boldsymbol{e_l}$ direction equation and the curvature κ_{nl} and κ_{gl} from the 3D-CST-boos governing equations yields a theory applicable to 2-D curved shocks, reproducing previous results. Calculations were performed using 3D-CST-boos and the method of Mölder (2015). The first-order flow parameters following the axisymmetric convex shock were found to be entirely consistent. Various 3-D shock shapes were analysed in this paper, with a distinct emphasis on their 3-D characteristics. The proposed 3D-CST-boos was then employed to determine the first-order flow parameters behind an elliptical convex shock. Further analysis was conducted on the flow field behind elliptical convex shocks under a non-uniform incoming flow and an incoming flow with a non-zero angle of attack.

Subsequently, a common 3-D concave shock was analysed, and its postshock parameters were calculated. The 3-D flow field behind the concave shock was determined using the LTOC method. The results near the concave shock of the flow field were compared with the theoretical results obtained from 3D-CST-boos, and the maximum error was found to be less than 3 %. The main reason for the error is that the LTOC method is not accurate enough to solve the 3-D flow field. The difference between the 3-D flow field generated by an elliptical concave shock and an axisymmetric concave shock (which is exactly the same as the shape of the elliptical shock's short or long half-axis) was elucidated. Furthermore, the gradient parameters of more intricate 3-D curved shocks, such as saddle-shaped and cubic surface shocks, were presented, and a brief analysis of the flow behind these complex 3-D shocks was provided. Because 3D-CST-boos is relatively terse, there are still many directions in which the theory can be extended. By analysing the first-order flow parameters behind 3-D curved shocks, more effective guidance can be provided for the design of supersonic flow fields. This includes the design of aerodynamic components that generate shocks, such as inlets or waveriders.

Funding. The authors would like to acknowledge the support of the National Natural Science Foundation of China (grant numbers U21B6003, U20A2069, 12302389 and 12372295).

Declaration of interests. The authors report no conflict of interest.

Appendix A. Coordinate transformation of Euler equations

Mass conservation equation:

$$\begin{aligned}\nabla\cdot(\rho\boldsymbol{V}) &= \nabla\cdot[\rho\,(V_l\boldsymbol{e_l}+V_m\boldsymbol{e_m}+V_n\boldsymbol{e_n})]\\ &= \boldsymbol{e_l}\frac{\partial(\rho V_l\boldsymbol{e_l}+\rho V_m\boldsymbol{e_m}+\rho V_n\boldsymbol{e_n})}{\partial l}\\ &\quad+\boldsymbol{e_m}\frac{\partial(\rho V_l\boldsymbol{e_l}+\rho V_m\boldsymbol{e_m}+\rho V_n\boldsymbol{e_n})}{\partial m}\\ &\quad+\boldsymbol{e_n}\frac{\partial(\rho V_l\boldsymbol{e_l}+\rho V_m\boldsymbol{e_m}+\rho V_n\boldsymbol{e_n})}{\partial n}=0.\end{aligned}\tag{A1}$$

https://doi.org/10.1017/jfm.2025.10859 Published online by Cambridge University Press

Decomposition calculation 1:

$$\begin{aligned}
\boldsymbol{e_l}\frac{\partial\left(\rho V_l\boldsymbol{e_l}+\rho V_m\boldsymbol{e_m}+\rho V_n\boldsymbol{e_n}\right)}{\partial l} &= \boldsymbol{e_l}\left[\frac{\partial\left(\rho V_l\boldsymbol{e_l}\right)}{\partial l}+\frac{\partial\left(\rho V_m\boldsymbol{e_m}\right)}{\partial l}+\frac{\partial\left(\rho V_n\boldsymbol{e_n}\right)}{\partial l}\right]\\
&= \boldsymbol{e_l}\left(0+0+0+\frac{\partial\rho}{\partial l}V_m\boldsymbol{e_m}+\frac{\partial V_m}{\partial l}\rho\boldsymbol{e_m}+\frac{\partial\boldsymbol{e_m}}{\partial l}\rho V_m+\frac{\partial\rho}{\partial l}V_n\boldsymbol{e_n}+\frac{\partial V_n}{\partial l}\rho\boldsymbol{e_n}+\frac{\partial\boldsymbol{e_n}}{\partial l}\rho V_n\right)\\
&= \rho V_m\frac{\partial\boldsymbol{e_m}}{\partial l}\boldsymbol{e_l}+\rho V_n\frac{\partial\boldsymbol{e_n}}{\partial l}\boldsymbol{e_l}\\
&= \rho V_m(-\kappa_{gl}\boldsymbol{e_l}+\tau_{gl}\boldsymbol{e_n})\boldsymbol{e_l}+\rho V_n(-\kappa_{nl}\boldsymbol{e_l}-\tau_{gl}\boldsymbol{e_m})\boldsymbol{e_l}\\
&= -\rho V_m\kappa_{gl}-\rho V_n\kappa_{nl}.
\end{aligned}\tag{A2}$$

Decomposition calculation 2:

$$\begin{aligned}
\boldsymbol{e_m}\frac{\partial\left(\rho V_l\boldsymbol{e_l}+\rho V_m\boldsymbol{e_m}+\rho V_n\boldsymbol{e_n}\right)}{\partial m} &= \boldsymbol{e_m}\left[\frac{\partial\left(\rho V_l\boldsymbol{e_l}\right)}{\partial m}+\frac{\partial\left(\rho V_m\boldsymbol{e_m}\right)}{\partial m}+\frac{\partial\left(\rho V_n\boldsymbol{e_n}\right)}{\partial m}\right]\\
&= \boldsymbol{e_m}\left(0+\frac{\partial V_l}{\partial m}\rho\boldsymbol{e_l}+0+\frac{\partial\rho}{\partial m}V_m\boldsymbol{e_m}+\frac{\partial V_m}{\partial m}\rho\boldsymbol{e_m}+\frac{\partial\boldsymbol{e_m}}{\partial m}\rho V_m+\frac{\partial\rho}{\partial m}V_n\boldsymbol{e_n}\right.\\
&\quad\left.+\frac{\partial V_n}{\partial m}\rho\boldsymbol{e_n}+\frac{\partial\boldsymbol{e_n}}{\partial m}\rho V_n\right)\\
&= \frac{\partial\rho}{\partial m}V_m+\frac{\partial V_m}{\partial m}\rho+\rho V_m\frac{\partial\boldsymbol{e_m}}{\partial m}\boldsymbol{e_m}+\rho V_n\frac{\partial\boldsymbol{e_n}}{\partial m}\boldsymbol{e_m}\\
&= \frac{\partial\rho}{\partial m}V_m+\frac{\partial V_m}{\partial m}\rho+\rho V_m(\kappa_{gm}\boldsymbol{e_l}+\kappa_{nm}\boldsymbol{e_n})\boldsymbol{e_m}+\rho V_n(-\kappa_{nm}\boldsymbol{e_m}-\tau_{gm}\boldsymbol{e_l})\boldsymbol{e_m}\\
&= \frac{\partial\rho}{\partial m}V_m+\frac{\partial V_m}{\partial m}\rho-\rho V_n\kappa_{nm}.
\end{aligned}\tag{A3}$$

Decomposition calculation 3:

$$\begin{aligned}
\boldsymbol{e_n}\frac{\partial(\rho V_l\boldsymbol{e_l}+\rho V_m\boldsymbol{e_m}+\rho V_n\boldsymbol{e_n})}{\partial n} &= \boldsymbol{e_n}\left[\frac{\partial(\rho V_l\boldsymbol{e_l})}{\partial n}+\frac{\partial(\rho V_m\boldsymbol{e_m})}{\partial n}+\frac{\partial(\rho V_n\boldsymbol{e_n})}{\partial n}\right]\\
&= \boldsymbol{e_n}\left(0+\frac{\partial V_l}{\partial n}\rho\boldsymbol{e_l}+0+\frac{\partial\rho}{\partial n}V_m\boldsymbol{e_m}+\frac{\partial V_m}{\partial n}\rho\boldsymbol{e_m}+\frac{\partial\boldsymbol{e_m}}{\partial n}\rho V_m+\frac{\partial\rho}{\partial n}V_n\boldsymbol{e_n}\right.\\
&\quad\left.+\frac{\partial V_n}{\partial n}\rho\boldsymbol{e_n}+\frac{\partial\boldsymbol{e_n}}{\partial n}\rho V_n\right)\\
&= \frac{\partial\rho}{\partial n}V_n+\frac{\partial V_n}{\partial n}\rho+\rho V_m\frac{\partial\boldsymbol{e_m}}{\partial n}\boldsymbol{e_n}+\rho V_n\frac{\partial\boldsymbol{e_n}}{\partial n}\boldsymbol{e_n}\\
&= \frac{\partial\rho}{\partial n}V_n+\frac{\partial V_n}{\partial n}\rho\\
&= \frac{\partial\rho}{\partial n}V_n+\frac{\partial V_n}{\partial n}\rho.
\end{aligned}\tag{A4}$$

The above decomposition calculations can be rearranged as

$$\rho\frac{\partial V_m}{\partial m}+\rho\frac{\partial V_n}{\partial n}+V_m\frac{\partial\rho}{\partial m}+V_n\frac{\partial\rho}{\partial n}-\rho V_n\kappa_{nm}-\rho V_n\kappa_{nl}-\rho V_m\kappa_{gl}=0.\tag{A5}$$

Momentum equation:

$$\rho\left(\boldsymbol{V}\cdot\boldsymbol{\nabla}\right)\cdot\boldsymbol{V}+\boldsymbol{\nabla}p=0.\tag{A6}$$

https://doi.org/10.1017/jfm.2025.10859 Published online by Cambridge University Press

Decomposition calculation 1:

$$
\begin{aligned}
(\boldsymbol{V}\cdot\nabla)\cdot\boldsymbol{V} &= V_l\frac{\partial \boldsymbol{V}}{\partial l}+V_m\frac{\partial \boldsymbol{V}}{\partial m}+V_n\frac{\partial \boldsymbol{V}}{\partial n}\\
&= V_l\frac{\partial(V_l\boldsymbol{e_l}+V_m\boldsymbol{e_m}+V_n\boldsymbol{e_n})}{\partial l}+V_m\frac{\partial(V_l\boldsymbol{e_l}+V_m\boldsymbol{e_m}+V_n\boldsymbol{e_n})}{\partial m}\\
&\quad+V_n\frac{\partial(V_l\boldsymbol{e_l}+V_m\boldsymbol{e_m}+V_n\boldsymbol{e_n})}{\partial n}\\
&= V_m\left(\frac{\partial V_m}{\partial m}\boldsymbol{e_m}+\frac{\partial \boldsymbol{e_m}}{\partial m}V_m+\frac{\partial V_n}{\partial m}\boldsymbol{e_n}+\frac{\partial \boldsymbol{e_n}}{\partial m}V_n\right)\\
&\quad+V_n\left(\frac{\partial V_l}{\partial n}\boldsymbol{e_l}+\frac{\partial V_m}{\partial n}\boldsymbol{e_m}+\frac{\partial V_n}{\partial n}\boldsymbol{e_n}\right)\\
&= V_m(\frac{\partial V_m}{\partial m}\boldsymbol{e_m}+(\kappa_{gm}\boldsymbol{e_l}+\kappa_{nm}\boldsymbol{e_n})V_m+\frac{\partial V_n}{\partial m}\boldsymbol{e_n}+(-\kappa_{nm}\boldsymbol{e_m}-\tau_{gm}\boldsymbol{e_l})V_n)\\
&\quad+V_n\left(\frac{\partial V_l}{\partial n}\boldsymbol{e_l}+\frac{\partial V_m}{\partial n}\boldsymbol{e_m}+\frac{\partial V_n}{\partial n}\boldsymbol{e_n}\right)\\
&= \boldsymbol{e_l}\left(V_n\frac{\partial V_l}{\partial n}+V_m^2\kappa_{gm}-V_mV_n\tau_{gm}\right)+\boldsymbol{e_m}\left(V_m\frac{\partial V_m}{\partial m}+V_n\frac{\partial V_m}{\partial n}-V_nV_m\kappa_{nm}\right)\\
&\quad+\boldsymbol{e_n}\left(V_n\frac{\partial V_n}{\partial n}+V_m\frac{\partial V_n}{\partial m}+V_m^2\kappa_{nm}\right).
\end{aligned}
\tag{A7}
$$

Decomposition calculation 2:

$$
\nabla \mathrm{p}=\boldsymbol{e_l}\frac{\partial p}{\partial l}+\boldsymbol{e_m}\frac{\partial p}{\partial m}+\boldsymbol{e_n}\frac{\partial p}{\partial n}. \tag{A8}
$$

The above decomposition calculations can be rearranged as

$$
\begin{aligned}
\boldsymbol{e_l}:&\rho V_n\frac{\partial V_l}{\partial n}+\rho V_m^2\kappa_{gm}-\rho V_mV_n\tau_{gm}+\frac{\partial p}{\partial l}=0,\\
\boldsymbol{e_m}:&\rho V_m\frac{\partial V_m}{\partial m}+\rho V_n\frac{\partial V_m}{\partial n}-\rho V_nV_m\kappa_{nm}+\frac{\partial p}{\partial m}=0,\\
\boldsymbol{e_n}:&\rho V_n\frac{\partial V_n}{\partial n}+\rho V_m\frac{\partial V_n}{\partial m}+\rho V_m^2\kappa_{nm}+\frac{\partial p}{\partial n}=0.
\end{aligned}
\tag{A9}
$$

Energy equation:

$$
\begin{aligned}
&\rho\,(\boldsymbol{V}\cdot\nabla)\left(h+\frac{V^2}{2}\right)=\rho\,(\boldsymbol{V}\cdot\nabla)\left(C_pT+\frac{V^2}{2}\right)=\rho\,(\boldsymbol{V}\cdot\nabla)\left(\frac{\gamma R}{\gamma-1}T+\frac{\boldsymbol{V}^2}{2}\right)\\
&=\rho\boldsymbol{V}\cdot\left[\frac{\partial\left(\frac{\gamma R}{\gamma-1}T+\frac{V^2}{2}\right)}{\partial l}\boldsymbol{e_l}+\frac{\partial\left(\frac{\gamma R}{\gamma-1}T+\frac{V^2}{2}\right)}{\partial m}\boldsymbol{e_m}+\frac{\partial\left(\frac{\gamma R}{\gamma-1}T+\frac{V^2}{2}\right)}{\partial n}\boldsymbol{e_n}\right]\\
&=\rho V_l\left(\frac{\gamma R}{\gamma-1}\frac{\partial T}{\partial l}+\frac{V_l\partial V_l}{\partial l}+\frac{V_m\partial V_m}{\partial l}+\frac{V_n\partial V_n}{\partial l}\right)
\end{aligned}
$$

https://doi.org/10.1017/jfm.2025.10859 Published online by Cambridge University Press

$$
\begin{aligned}
&+\rho V_m\left(\frac{\gamma R}{\gamma-1}\frac{\partial T}{\partial m}+\frac{V_l\partial V_l}{\partial m}+\frac{V_m\partial V_m}{\partial m}+\frac{V_n\partial V_n}{\partial m}\right)\\
&+\rho V_n\left(\frac{\gamma R}{\gamma-1}\frac{\partial T}{\partial n}+\frac{V_l\partial V_l}{\partial n}+\frac{V_m\partial V_m}{\partial n}+\frac{V_n\partial V_n}{\partial n}\right)\\
&=\frac{\gamma V_m}{\gamma-1}\left(\frac{\partial p}{\partial m}-\frac{p}{\rho}\frac{\partial \rho}{\partial m}\right)\rho V_m^2\frac{\partial V_m}{\partial m}+\rho V_m V_n\frac{\partial V_n}{\partial m}\\
&+\frac{\gamma V_n}{\gamma-1}\left(\frac{\partial p}{\partial n}-\frac{p}{\rho}\frac{\partial \rho}{\partial n}\right)+\rho V_n V_m\frac{\partial V_m}{\partial n}+\rho V_n^2\frac{\partial V_n}{\partial n}=0.
\end{aligned}
\tag{A10}
$$

The partial derivative of the equation of state $P=\rho RT$ along the $\boldsymbol{e_l}$, $\boldsymbol{e_m}$, and $\boldsymbol{e_n}$ directions is expressed as follows:

$$
\begin{aligned}
\boldsymbol{e_l}:&\frac{\partial p}{\partial l}=\frac{\partial \rho}{\partial l}RT+\rho R\frac{\partial T}{\partial l},\\
\boldsymbol{e_m}:&\frac{\partial p}{\partial m}=\frac{\partial \rho}{\partial m}RT+\rho R\frac{\partial T}{\partial m},\\
\boldsymbol{e_n}:&\frac{\partial p}{\partial n}=\frac{\partial \rho}{\partial n}RT+\rho R\frac{\partial T}{\partial n}.
\end{aligned}
\tag{A11}
$$

Appendix B. Derivation of 3D-CST-boos equations (part one)

Observe the eight (2.26)–(2.33), they are independent in the $\boldsymbol{e_l}$ direction and the $\boldsymbol{e_m}$ direction, and then deduce the $\boldsymbol{e_l}$ direction as an example. Write the (2.26), (2.28) and (2.32) in the following form:

$$X_1=R_{2L}+V_{2NL}, \tag{B1}$$

$$X_2=A_2P_{2L}+B_2R_{2L}+2B_2V_{2NL}, \tag{B2}$$

$$X_3=C_2P_{2L}-C_2R_{2L}+D_2V_{2NL}. \tag{B3}$$

When the incoming flow parameters are determined, the flow parameters in front of the shock are all known. In order to facilitate the subsequent derivation of the equation, the following coefficients are defined:

$$
\left.
\begin{aligned}
X_1&=R_{1L}+V_{1NL},\\
X_2&=A_1P_{1L}+B_1R_{1L}+2B_1V_{1NL},\\
X_3&=C_1P_{1L}-C_1R_{1L}+D_1V_{1NL}.
\end{aligned}
\right\}
\tag{B4}
$$

Write the above equation in matrix form,

$$
\left(\begin{array}{ccc|c}
1 & 0 & 1 & X_1\\
B_2 & A_2 & 2B_2 & X_2\\
-C_2 & C_2 & D_2 & X_3
\end{array}\right)\rightarrow
\left(\begin{array}{ccc|c}
1 & 0 & 1 & X_1\\
0 & A_2 & B_2 & X_2-X_1B_2\\
0 & C_2 & D_2+C_2 & X_3+X_1C_2
\end{array}\right)
$$

$$
\rightarrow\left(\begin{array}{ccc|c}
1 & 0 & 1 & X_1\\
0 & A_2 & B_2 & X_2-X_1B_2\\
0 & 0 & D_2+C_2+\dfrac{-B_2C_2}{A_2} & X_3+X_1C_2-\dfrac{C_2}{A_2}(X_2-X_1B_2)
\end{array}\right)
$$

https://doi.org/10.1017/jfm.2025.10859 Published online by Cambridge University Press

$$\rightarrow \left(\begin{array}{ccc|c} 1 & 0 & 1 & X_1 \\ 0 & A_2 & B_2 & X_2 - X_1 B_2 \\ 0 & 0 & 1 & \dfrac{A_2\,(X_3 + X_1 C_2)}{A_2 D_2 + A_2 C_2 - B_2 C_2} - \dfrac{C_2\,(X_2 - X_1 B_2)}{A_2 D_2 + A_2 C_2 - B_2 C_2} \end{array}\right)$$

$$\rightarrow \left(\begin{array}{ccc|c} 1 & 0 & 0 & X_1 - \dfrac{A_2\,(X_3 + X_1 C_2)}{A_2 D_2 + A_2 C_2 - B_2 C_2} + \dfrac{C_2\,(X_2 - X_1 B_2)}{A_2 D_2 + A_2 C_2 - B_2 C_2} \\ 0 & A_2 & 0 & X_2 - X_1 B_2 - \dfrac{B_2 A_2\,(X_3 + X_1 C_2) + B_2 C_2\,(X_2 - X_1 B_2)}{A_2 D_2 + A_2 C_2 - B_2 C_2} \\ 0 & 0 & 1 & \dfrac{A_2\,(X_3 + X_1 C_2)}{A_2 D_2 + A_2 C_2 - B_2 C_2} - \dfrac{C_2\,(X_2 - X_1 B_2)}{A_2 D_2 + A_2 C_2 - B_2 C_2} \end{array}\right). \tag{B5}$$

After diagonalizing the left-hand side of the above matrix, dimensionless expressions for P_{2L}, R_{2L} and V_{2NL} can be written directly:

$$\begin{aligned} P_{2L} &= \frac{X_2 - X_1 B_2}{A_2} - \frac{B_2 A_2\,(X_3 + X_1 C_2) + B_2 C_2\,(X_2 - X_1 B_2)}{A_2^2 D_2 + A_2^2 C_2 - A_2 B_2 C_2} \\ &= \left(-\frac{B_2}{A_2} + \frac{-B_2 A_2 C_2 - B_2^2 C_2}{A_2^2 D_2 + A_2^2 C_2 - A_2 B_2 C_2}\right) X_1 + \left(\frac{1}{A_2} + \frac{B_2 C_2}{A_2^2 D_2 + A_2^2 C_2 - A_2 B_2 C_2}\right) X_2 \\ &\quad + \frac{-B_2 A_2}{A_2^2 D_2 + A_2^2 C_2 - A_2 B_2 C_2} X_3, \end{aligned} \tag{B6}$$

$$\begin{aligned} R_{2L} &= \left(1 + \frac{-A_2 C_2 - B_2 C_2}{A_2 D_2 + A_2 C_2 - B_2 C_2}\right) X_1 + \frac{C_2}{A_2 D_2 + A_2 C_2 - B_2 C_2} X_2 \\ &\quad - \frac{A_2}{A_2 D_2 + A_2 C_2 - B_2 C_2} X_3, \end{aligned} \tag{B7}$$

$$\begin{aligned} V_{2NL} &= \frac{A_2 C_2 + B_2 C_2}{A_2 D_2 + A_2 C_2 - B_2 C_2} X_1 - \frac{C_2}{A_2 D_2 + A_2 C_2 - B_2 C_2} X_2 \\ &\quad + \frac{A_2}{A_2 D_2 + A_2 C_2 - B_2 C_2} X_3. \end{aligned} \tag{B8}$$

Substituting (B4) into the (B6)–(B8) yields the following expression:

$$\begin{aligned} P_{2L} &= \left(-\frac{B_2}{A_2} + \frac{-B_2 A_2 C_2 - B_2^2 C_2 + B_1 B_2 C_2}{A_2^2 D_2 + A_2^2 C_2 - A_2 B_2 C_2} + \frac{B_1}{A_2} + \frac{B_2 C_1}{A_2 D_2 + A_2 C_2 - B_2 C_2}\right) R_{1L} \\ &\quad + \left(-\frac{B_2}{A_2} + \frac{-B_2 A_2 C_2 - B_2^2 C_2}{A_2^2 D_2 + A_2^2 C_2 - A_2 B_2 C_2} + \frac{2B_1}{A_2} + \frac{2B_1 B_2 C_2 - B_2 A_2 D_1}{A_2^2 D_2 + A_2^2 C_2 - A_2 B_2 C_2}\right) V_{1NL} \\ &\quad + \left(\frac{A_1}{A_2} + \frac{A_1 B_2 C_2 - A_2 B_2 C_1}{A_2^2 D_2 + A_2^2 C_2 - A_2 B_2 C_2}\right) P_{1L}, \end{aligned} \tag{B9}$$

https://doi.org/10.1017/jfm.2025.10859 Published online by Cambridge University Press

$$R_{2L} = \left(1 + \frac{-A_2C_2 - B_2C_2}{A_2D_2 + A_2C_2 - B_2C_2} + \frac{B_1C_2 + A_2C_1}{A_2D_2 + A_2C_2 - B_2C_2}\right) R_{1L} + \frac{C_2A_1 - A_2C_1}{A_2D_2 + A_2C_2 - B_2C_2} P_{1L} + \left(1 + \frac{-A_2C_2 - B_2C_2 + 2B_1C_2 - A_2D_1}{A_2D_2 + A_2C_2 - B_2C_2}\right) V_{1NL}, \tag{B10}$$

$$V_{2NL} = \frac{A_2C_2 + B_2C_2 - B_1C_2 - A_2C_1}{A_2D_2 + A_2C_2 - B_2C_2} R_{1L} + \frac{-A_1C_2 + A_2C_1}{A_2D_2 + A_2C_2 - B_2C_2} P_{1L} + \frac{A_2C_2 + B_2C_2 - 2B_1C_2 + A_2D_1}{A_2D_2 + A_2C_2 - B_2C_2} V_{1NL}. \tag{B11}$$

Using the (2.36), (2.38) and (2.40) in the $\boldsymbol{e_m}$ direction, the above derivation process will be repeated to obtain the P_{2M}, R_{2M} and V_{2NM} parameters:

$$P_{2M} = \left(-\frac{B_2}{A_2} + \frac{-B_2A_2C_2 - B_2^2C_2 + B_1B_2C_2}{A_2^2D_2 + A_2^2C_2 - A_2B_2C_2} + \frac{B_1}{A_2} + \frac{B_2C_1}{A_2D_2 + A_2C_2 - B_2C_2}\right) R_{1M} + \left(-\frac{B_2}{A_2} + \frac{-B_2A_2C_2 - B_2^2C_2}{A_2^2D_2 + A_2^2C_2 - A_2B_2C_2} + \frac{2B_1}{A_2} + \frac{2B_1B_2C_2 - B_2A_2D_1}{A_2^2D_2 + A_2^2C_2 - A_2B_2C_2}\right) V_{1NM} + \left(\frac{A_1}{A_2} + \frac{A_1B_2C_2 - A_2B_2C_1}{A_2^2D_2 + A_2^2C_2 - A_2B_2C_2}\right) P_{1M}, \tag{B12}$$

$$R_{2M} = \left(1 + \frac{-A_2C_2 - B_2C_2}{A_2D_2 + A_2C_2 - B_2C_2} + \frac{B_1C_2 + A_2C_1}{A_2D_2 + A_2C_2 - B_2C_2}\right) R_{1M} + \frac{C_2A_1 - A_2C_1}{A_2D_2 + A_2C_2 - B_2C_2} P_{1M} + \left(1 + \frac{-A_2C_2 - B_2C_2 + 2B_1C_2 - A_2D_1}{A_2D_2 + A_2C_2 - B_2C_2}\right) V_{1NM}, \tag{B13}$$

$$V_{2NM} = \frac{A_2C_2 + B_2C_2 - B_1C_2 - A_2C_1}{A_2D_2 + A_2C_2 - B_2C_2} R_{1M} + \frac{-A_1C_2 + A_2C_1}{A_2D_2 + A_2C_2 - B_2C_2} P_{1M} + \frac{A_2C_2 + B_2C_2 - 2B_1C_2 + A_2D_1}{A_2D_2 + A_2C_2 - B_2C_2} V_{1NM}. \tag{B14}$$

Further arrange (B9)–(B14):

$$P_{2L} = J_1R_{1L} + J_2V_{1NL} + J_3P_{1L}, \tag{B15}$$
$$P_{2M} = J_1R_{1M} + J_2V_{1NM} + J_3P_{1M}, \tag{B16}$$
$$R_{2L} = (1 + K_1)R_{1L} + K_2P_{1L} + K_3V_{1NL}, \tag{B17}$$
$$R_{2M} = (1 + K_1)R_{1M} + K_2P_{1M} + K_3V_{1NM}, \tag{B18}$$
$$V_{2NL} = -K_1R_{1L} - K_2P_{1L} - K_3V_{1NL}, \tag{B19}$$
$$V_{2NM} = -K_1R_{1M} - K_2P_{1M} - K_3V_{1NM}. \tag{B20}$$

https://doi.org/10.1017/jfm.2025.10859 Published online by Cambridge University Press

The coefficients can be expressed as

$$\left.\begin{aligned} J_1 &= \left(-\frac{B_2}{A_2}+\frac{-B_2A_2C_2-B_2^2C_2+B_1B_2C_2}{A_2^2D_2+A_2^2C_2-A_2B_2C_2}+\frac{B_1}{A_2}+\frac{B_2C_1}{A_2D_2+A_2C_2-B_2C_2}\right),\\ J_2 &= \left(-\frac{B_2}{A_2}+\frac{-B_2A_2C_2-B_2^2C_2}{A_2^2D_2+A_2^2C_2-A_2B_2C_2}+\frac{2B_1}{A_2}+\frac{2B_1B_2C_2-B_2A_2D_1}{A_2^2D_2+A_2^2C_2-A_2B_2C_2}\right),\\ J_3 &= \left(\frac{A_1}{A_2}+\frac{A_1B_2C_2-A_2B_2C_1}{A_2^2D_2+A_2^2C_2-A_2B_2C_2}\right),\\ K_1 &= \left(\frac{-A_2C_2-B_2C_2}{A_2D_2+A_2C_2-B_2C_2}+\frac{B_1C_2+A_2C_1}{A_2D_2+A_2C_2-B_2C_2}\right),\\ K_2 &= \left(\frac{B_1C_2+A_2C_1}{A_2D_2+A_2C_2-B_2C_2}\right),\\ K_3 &= \left(\frac{-A_2C_2-B_2C_2+2B_1C_2-A_2D_1}{A_2D_2+A_2C_2-B_2C_2}\right). \end{aligned}\right\} \tag{B21}$$

Appendix C. Derivation of 3D-CST-boos equations (part two)

The expression of P_{2N} is derived using (2.10):

$$\frac{\gamma V_m}{\gamma-1}\left(\frac{\partial p}{\partial m}-\frac{p}{\rho}\frac{\partial \rho}{\partial m}\right)+\rho V_m^2\frac{\partial V_m}{\partial m}+\rho V_mV_n\frac{\partial V_n}{\partial m} +\frac{\gamma V_n}{\gamma-1}\left(\frac{\partial p}{\partial n}-\frac{p}{\rho}\frac{\partial \rho}{\partial n}\right)+\rho V_nV_m\frac{\partial V_m}{\partial n}+\rho V_n^2\frac{\partial V_n}{\partial n}=0. \tag{C1}$$

Use (2.6) to replace $(\partial\rho/\partial n)$ in (C1):

$$\begin{aligned} &\frac{\gamma V_m}{\gamma-1}\left(\frac{\partial p}{\partial m}-\frac{p}{\rho}\frac{\partial \rho}{\partial m}\right)+\rho V_m^2\frac{\partial V_m}{\partial m}+\rho V_mV_n\frac{\partial V_n}{\partial m}+\frac{\gamma V_n}{\gamma-1}\frac{\partial p}{\partial n}+\rho V_nV_m\frac{\partial V_m}{\partial n}+\rho V_n^2\frac{\partial V_n}{\partial n}\\ &\quad+\frac{\gamma}{\gamma-1}\frac{p}{\rho}\left(\rho\frac{\partial V_m}{\partial m}+\rho\frac{\partial V_n}{\partial n}+V_m\frac{\partial \rho}{\partial m}-\rho V_n\kappa_{nm}-\rho V_n\kappa_{nl}-\rho V_m\kappa_{gl}\right)\\ &=\frac{\gamma V_m}{\gamma-1}\frac{\partial p}{\partial m}+\rho V_m^2\frac{\partial V_m}{\partial m}+\rho V_mV_n\frac{\partial V_n}{\partial m}+\frac{\gamma V_n}{\gamma-1}\frac{\partial p}{\partial n}+\rho V_nV_m\frac{\partial V_m}{\partial n}+\rho V_n^2\frac{\partial V_n}{\partial n}\\ &\quad+\frac{\gamma p}{\gamma-1}\left(\frac{\partial V_m}{\partial m}-V_n\kappa_{nm}-V_n\kappa_{nl}-V_m\kappa_{gl}\right)+\frac{\gamma p}{\gamma-1}\frac{\partial V_n}{\partial n}=0. \end{aligned} \tag{C2}$$

Use (2.8) and (2.9) to replace $(\partial V_m/\partial n)$ and $(\partial V_n/\partial n)$ in (C2):

$$\begin{aligned} &\frac{\gamma V_m}{\gamma-1}\frac{\partial p}{\partial m}+\rho V_m^2\frac{\partial V_m}{\partial m}+\rho V_mV_n\frac{\partial V_n}{\partial m}+\frac{\gamma V_n}{\gamma-1}\frac{\partial p}{\partial n}\frac{\gamma p}{\gamma-1}\left(\frac{\partial V_m}{\partial m}-V_n\kappa_{nm}-V_n\kappa_{nl}-V_m\kappa_{gl}\right)\\ &\quad-\left(\frac{1}{\rho V_n}\frac{\gamma p}{\gamma-1}+V_n\right)\left(\rho V_m\frac{\partial V_n}{\partial m}+\rho V_m^2\kappa_{nm}+\frac{\partial p}{\partial n}\right)\\ &\quad-V_m\left(\rho V_m\frac{\partial V_m}{\partial m}-\rho V_nV_m\kappa_{nm}+\frac{\partial p}{\partial m}\right)\\ &=\frac{V_m}{\gamma-1}\frac{\partial p}{\partial m}+\frac{\gamma p}{\gamma-1}\frac{\partial V_m}{\partial m}-\frac{V_m}{V_n}\frac{\gamma p}{\gamma-1}\frac{\partial V_n}{\partial m}+\left(\frac{V_n}{\gamma-1}-\frac{1}{\rho V_n}\frac{\gamma p}{\gamma-1}\right)\frac{\partial p}{\partial n} \end{aligned}$$

https://doi.org/10.1017/jfm.2025.10859 Published online by Cambridge University Press

$$-\frac{\gamma p}{\gamma-1}\left(V_n\kappa_{nm}+V_n\kappa_{nl}+V_m\kappa_{gl}\right)-\frac{1}{V_n}\frac{\gamma p}{\gamma-1}V_m^2\kappa_{nm}$$
$$=\frac{1}{\gamma-1}\left[V_m\frac{\partial p}{\partial m}+\gamma p\frac{\partial V_m}{\partial m}-\frac{\gamma p V_m}{V_n}\frac{\partial V_n}{\partial m}+\left(V_n-\frac{\gamma p}{\rho V_n}\right)\frac{\partial p}{\partial n}\right]$$
$$-\frac{1}{\gamma-1}\left[\gamma p\left(V_n\kappa_{nl}+V_m\kappa_{gl}\right)+\frac{\gamma p\left(V_m^2+V_n^2\right)}{V_n}\kappa_{nm}\right]=0. \tag{C3}$$

The expression for P_N is further derived:

$$\frac{\partial p}{p\partial n}=\frac{\left[\frac{V_m}{V_n}\frac{\partial p}{p\partial m}+\frac{\gamma V_m}{V_n}\frac{\partial V_m}{V_m\partial m}-\frac{\gamma V_m}{V_n}\frac{\partial V_n}{V_n\partial m}-\frac{\gamma}{V_n}\left(V_n\kappa_{nl}+V_m\kappa_{gl}\right)-\frac{\gamma\left(V_m^2+V_n^2\right)}{V_n^2}\kappa_{nm}\right]}{\left(\frac{\gamma p}{\rho V_n^2}-1\right)}. \tag{C4}$$

Further arrange (C4):

$$P_{2N}=L_1P_{2M}+L_2\left(V_{2MM}-V_{2NM}\right)-L_2\kappa_{gl}-L_3\left(\kappa_{nl}+\kappa_{nm}\right)-L_4\kappa_{nm}; \tag{C5}$$

where the coefficients can be expressed as

$$\left.\begin{aligned}L_1&=\frac{V_m}{V_n}/\left(\frac{\gamma p}{\rho V_n^2}-1\right),\quad L_2=\frac{\gamma V_m}{V_n}/\left(\frac{\gamma p}{\rho V_n^2}-1\right),\\ L_3&=\gamma/\left(\frac{\gamma p}{\rho V_n^2}-1\right),\quad L_4=\frac{\gamma V_m^2}{V_n^2}/\left(\frac{\gamma p}{\rho V_n^2}-1\right).\end{aligned}\right\} \tag{C6}$$

References

Best, J.P. 1991 A generalisation of the theory of geometrical shock dynamics. *Shock Waves* **1**, 251–273.

Cheng, W.H. 2006 *Differential Geometry*, vol. 6, pp. 229–231. Peking University Press.

Chen, S.S. 2024 Deformation modes and key technologies of aerodynamic layout design for morphing aircraft: review. *Acta Aeronaut. Astronaut. Sin.* **45** (6), 7–53.

Crocco, R. 1937 Singolarita della corrente gassosa iperacustica nellinterno di una prora a diedro. *Congres. Dell Unione Mat. Ital.* **15**, 597–615.

Emanuel, G. 1988 Shock wave derivatives. *Phys. Fluids* **31**, 3625–3633.

Emanuel, G. 2019 Derivatives on the downstream side of a moving, curved shock. *J. Eng. Math.* **117**, 79–105.

Emanuel, G. & Mölder, S. 2021 Three-dimensional curved shock theory. *Shock Waves* **32**, 129–146.

Filippi, A.A. 2018 Streamlines behind curved shock waves in axisymmetric flow fields. *Shock Waves* **28**, 785–793.

Hayes, W.D. 1959 *Hypersonic Flow Theory*. Academic Press.

Hornung, H.G. 1998 Gradients at a curved shock in reacting flow. *Shock Waves* **8** (1), 11–21.

Hornung, H.G. 2010 Deriving features of reacting hypersonic flow from gradients at a curved shock. *AIAA J.* **48** (2), 287–296.

Kanwal, R.P. 1959 On curved shock waves in three-dimensional gas flows. *Q. Appl. Math.* **16**, 361–372.

Lin, C.C. 1948 On the flow behind curved shocks. *Stud. Appl. Math.* **27**, 105–129.

Li, D. 2018 A review of modelling and analysis of morphing wings. *Prog. Aerosp. Sci.* **100**, 46–62.

Mölder, S. 2015 Curved shock theory. *Shock Waves* **26** (4), 1–17.

Pant, J.C. 1971 Reflection of a curved shock from a straight rigid boundary. *Phys. Fluids* **14**, 534–538.

Serrin, J. 1959 Mathematical principles of classical fluid mechanics. In *Encyclopedia of Physics* (ed. S. Flügge), vol. VIII–1.

Shi, C.G. 2020 Second-order curved shock theory. *J. Fluid Mech.* **A21**, 89–125.

Shi, C.G. 2021 Method of curved-shock characteristics with application to inverse design of supersonic flowfields. *J. Fluid Mech.* **A36**, 920.

Tembharey, D.J. 1973 A note on Beltrami and complex-lamellar flows behind a three-dimensional curved gas dynamic shock wave. *Q. Appl. Math.* **31**, 253–255.

Thomas, T.Y. 1947 On curved shock waves. *J. Math. Phys.* **26** (14), 62–68.

https://doi.org/10.1017/jfm.2025.10859 Published online by Cambridge University Press

YOU, Y.C. 2006 Invetigation of internal waverider-derived hypersonic inlet. *J. Propuls. Technol.* **27** (3), 252–259.

ZHANG, T. 2023*a* Reflection and transition of planar curved shock waves. *J. Fluid Mech.* **A11**, 959.

ZHANG, T. 2023*b* Mach reflection of three-dimensional curved shock waves on V-shaped blunt leading edges. *J. Fluid Mech.* **A45**, 975.

ZHENG, X.G. 2020*a* Multiple osculating cones' waverider design method for ruled shock surfaces. *AIAA J.* **58** (2), 854–866.

ZHENG, X.G. 2020*b* Local-turning osculating cones method for waverider design. **58** (8), *AIAA J.* 3499–3513.

ZHANG, R. 2024 Progress in trajectory design and optimization for hypersonic morphing aircraft. *Tact. Missile Technol.* **04**, 30–40.

ZHEN, Z.Y. 2022 Research progress on intelligent deformation and flight control technology of morphing aircraft. *J. Nanjing Univ. Aeronaut. Astronaut.* **54** (6), 995–1006.

https://doi.org/10.1017/jfm.2025.10859 Published online by Cambridge University Press